EXPERIMENTAL STUDIES OF THE DRAG OF AN AXISYMMETRIC SUBMARINE HULL

By

John Lindsley Freudenthal

A Thesis
Submitted to the Faculty of
Mississippi State University
in Partial Fulfillment of the Requirements
for the Degree of Master of Science
in Aerospace Engineering
in the Department of Aerospace Engineering

Mississippi State, Mississippi

December 2002

EXPERIMENTAL STUDIES OF THE DRAG OF AN

AXISYMMETRIC SUBMARINE HULL

By

John Lindsley Freudenthal

Approved:

David H. Bridges
Associate Professor of Aerospace Engineering (Director of Thesis)

Boyd Gatlin
Associate Professor, Interim Head and Graduate Coordinator of the Department of Aerospace Engineering

Keith Koenig
Professor of Aerospace Engineering
(Committee Member)

Z. U. A. Warsi
Professor of Aerospace Engineering
(Committee Member)

A. Wayne Bennett
Dean of the College of Engineering

Name: John Lindsley Freudenthal

Date of Degree: December 13, 2002

Institution: Mississippi State University

Major Field: Aerospace Engineering

Major Professor: Dr. David H. Bridges

Title of Study: EXPERIMENTAL STUDIES OF THE DRAG OF AN AXISYMMETRIC SUBMARINE HULL

Pages in Study: 79

Candidate for Degree of Master of Science

The purpose of these studies was to measure the drag coefficient of a small model submarine to add data to a Reynolds number study. First, a laser Doppler velocimeter (LDV) was used to measure the flow characteristics of the Mississippi State University water tunnel. The velocity and turbulence intensity profiles were measured for a range of freestream velocities of 8.6 m/s to 10.7 m/s. Several wake velocity profiles were taken for a model submarine at downstream distances of $x/d = 10$ to $x/d = 28$, with a freestream velocity of 8.6 m/s. A formula for the drag coefficient that uses only mean velocity measurements in the wake was derived for an axisymmetric body using the assumptions of a self-similar wake and a power law behavior of the wake scales. The experimental drag coefficient results are compared to computational fluid dynamic (CFD) solutions.

DEDICATION

To Mom and Dad

ACKNOWLEDGEMENTS

I wish to express my gratitude to Dr. David Bridges for his guidance and support throughout this project. I would also like to recognize Dr. Keith Koenig's support in both the theoretical and practical aspects of this research. I also would like to thank Jim Schrock for his extensive help with reassembling the water tunnel and troubleshooting all of its problems. A number of students (whether they worked for the Department or not) helped out along the way. In particular, I would like to thank Viva Austin for her enthusiastic willingness to help in any possible way.

This research would not have been possible without the funding by the Office of Naval Research DEPSCoR Grant No. N00014-99-1-0534. Dr. L. Patrick Purtell was the program monitor.

I would like to thank my fiancé, Sharon Johnston, for her encouragement and inspiration. I cannot imagine having finished this thesis without her influence. She helped me to see that I could not carry my burdens alone, but that I must give them to God. God has used my time at MSU to bring me back into a closer relationship with Him. This is the greatest lesson that I carry from this place.

I would like to thank my parents and Sharon's parents for their support and encouragement. Also, the support of the entire Aerospace Department "family" has been great—I have many new friends.

TABLE OF CONTENTS

CHAPTER Page

LIST OF TABLES

LIST OF FIGURES

FIGURE Page

LIST OF SYMBOLS

B	systematic uncertainty
b	wake half-width parameter
C_D	drag coefficient
$\Delta C_{D,p}$	drag coefficient contribution of pressure gradient
c_l	power law constant of proportionality for wake length scale
c_p	pressure coefficient
c_{p_0}	pressure coefficient outside of wake
c_{p_w}	pressure coefficient within wake
c_u	power law constant of proportionality for wake velocity scale
D	drag force
d	maximum body diameter
$d\underset{\sim}{S}$	surface element vector
$\hat{e}$	unit vector
F_p	pressure reaction force
H	total head
L	length of test section
L_{sub}	length of submarine model
l_0	wake length scale
P	random uncertainty
p	pressure
p_∞	pressure in freestream
p_0	pressure outside of wake
R	radius of control volume, disk, test section
t	time

U,V,W	cartesian velocity components
u,v,w	polar cylindrical velocity components
u',v',w'	polar cylindrical velocity fluctuating components
U	total uncertainty
U_0	velocity outside of wake
U_∞	velocity in freestream
$\underset{\sim}{u}$	velocity vector
u_0	wake velocity scale
$\forall$	control volume
$\forall_{body}$	volume of body
x,θ,r	polar cylindrical coordinates
x,y,z	cartesian coordinates
x_0	curve fit origin
z_{cl}	centerline of test section, traverse coordinate system
z_0	centerline of wake, from curve fit
δ_1	wake displacement thickness
Ω	motor input speed
μ	absolute viscosity
ν	kinematic viscosity
ρ	density
$\underset{\approx}{\tau}$	viscous stress tensor

CHAPTER I

INTRODUCTION

In recent years, the study of Reynolds number effects has become an increasingly important area of research. The extrapolation of data from a large experimental model to a full-scale prototype is extremely critical in predicting the performance of the prototype. Often the large model is still much smaller than the prototype. This is particularly true of naval vessels, including submarines. The Office of Naval Research funded a Reynolds number study to examine the capability of computational fluid dynamics (CFD) solutions to track large changes in Reynolds number. Three length scales of submarine hull forms were to be used in this study. A small model was to be constructed and tested in a water tunnel facility located at Mississippi State University. This model was to be identical in shape to a model tested in the U. S. Navy's Large Cavitation Channel (LCC), but the LCC model was to be over twenty times larger. The flow conditions of speed and pressure were to be the same in both experiments. CFD solutions were to be obtained for the small and large models, as well as for the full-scale submarine, which is over twenty times larger than the LCC model. It was hoped that the information obtained concerning how well the CFD solutions tracked the changes in Reynolds number when going from small model to large model would be useful in predicting how well the CFD solutions would track the next jump in order of Reynolds number magnitude when going from the large LCC model to the full-scale submarine. The objective of the current experiment was to obtain drag coefficient measurements of the smaller model submarine.

The Mississippi State University Department of Aerospace Engineering has performed hydrodynamic research in conjunction with the United States Navy for several years. The water tunnel in the Mississippi State Patterson Engineering Laboratories has been renovated to perform research work with the LCC. The first phase of research studied the effect of pressure tap hole size on static pressure measurements. After this first phase of testing, the water tunnel needed many repairs. The protective coating was replaced in many sections of the water tunnel. Also, the modification of the interior drive shaft bearing assembly and the addition of a reverse thrust bearing solved a problem that had developed with the bearings being burned out during operation. These modifications were completed before the current experiment was undertaken.

The Aerospace Engineering Department acquired a Laser Doppler Velocimeter (LDV) for use with the water tunnel, among other things. A calibration device consisting of a precisely controlled rotating disk was built for the LDV. Once the water tunnel was operational, the LDV was used to measure the flow characteristics of the water tunnel test section. After these tests were completed, a submarine model was mounted in the test section and wake velocity profiles were measured at several stations downstream. The drag coefficient of the submarine model was then computed using these wake velocity profiles. The calculated drag coefficients of the model submarine were in fairly good agreement with the CFD solutions. During the final stages of the experiment, a section of the water tunnel failed under pressure, effectively ending the experiment.

CHAPTER II

BACKGROUND

2.1 Total-Head Loss Measurement of the Drag of a Body

The classical approach to the drag measurement of a body has been to use a pitot probe to measure the total pressure distribution of the wake behind an experimental model. Two of the earliest methods were derived by Betz and by Jones, as discussed in *Modern Developments in Fluid Dynamics* [1]. Betz was the first to develop the technique of determining the drag of an airplane wing by measuring the pressure distribution of the wake at a short distance behind the wing's trailing edge. From the momentum equation, the drag of a wing can be calculated using the flow properties through two parallel planes at right angles to the mean flow:

$$D = \iint\left(p_1 + \rho U_1^2 \right) dS_1 - \iint\left(p_2 + \rho U_2^2 \right) dS_2 \ , \tag{2.1}$$

where the subscripts 1 and 2 denote the front plane and rear plane respectively. Betz introduced the total-head equations and a hypothetical flow to transform the above equation to an integral requiring measurements on the rear plane only:

$$\begin{aligned} D = & \iint_T \left(H_1 - H_2 \right) dS + \frac{1}{2}\rho \iint_T \left(U_2^* - U_2 \right)\left(U_2^* + U_2 - 2U_0 \right) dS + \\ & + \frac{1}{2}\rho \iint \left\{ \left(V_2^2 + W_2^2 \right) - \left(V_1^2 + W_1^2 \right) \right\} dS \ , \end{aligned} \tag{2.2}$$

where

$$U_2 = \sqrt{\frac{2(H_2 - p_2)}{\rho}}, \tag{2.3}$$

and

$$U_2^* = \sqrt{\frac{2(H_1 - p_2)}{\rho}}, \tag{2.4}$$

and the region T is the region of the wake only. The sum of the first two integrals of equation (2.2) yields the profile drag, and the third integral yields the induced drag. The second term in equation (2.2) is a correction factor that is important in regions close to the body. It is small when the measurement plane is at a considerable distance from the body. If there is no lift being produced by the body and the measurement plane is at a certain distance downstream of the body, the profile drag is simply the integration of the head deficit of the wake:

$$D = \iint_T (H_1 - H_2)\, dS\,. \tag{2.5}$$

B. M. Jones developed a similar method using measurements in a plane far downstream of a body. For a body at zero-lift conditions, at a certain distance downstream the pressure is uniformly equal to the freestream pressure p_∞ and the velocity is uniformly equal to the freestream velocity U_∞, except in the wake. The profile drag of the body is simply an integration over the wake region:

$$D = \rho \iint U_3 (U_\infty - U_3)\, dS_3\,, \tag{2.6}$$

where U_3 is the velocity in area element dS_3 of the wake. The total head at this downstream plane is

$$H_2 = \frac{1}{2}\rho U_3^2 + p_\infty \,. \tag{2.7}$$

Defining the function g such that

$$g = \left[1 - \frac{\left(H_\infty - H_2\right)}{\frac{1}{2}\rho U_\infty^2}\right], \tag{2.8}$$

equation (2.6) reduces to the form

$$D = \frac{1}{2}\rho U_\infty^2 \iint 2g^{1/2}\left(1 - g^{1/2}\right) dS_3 \,. \tag{2.9}$$

At a certain distance downstream of the body, $H_2 \to H_\infty$ and $g \to 1$, and the above equation (2.9) can be written approximately

$$D = \frac{1}{2}\rho U_\infty^2 \iint \left(1 - g\right) dS_3 = \iint \left(H_\infty - H_2\right) dS_3 \,, \tag{2.10}$$

which is the same form as equation (2.5).

2.2 Momentum Defect Measurement of the Drag of an Axisymmetric Body

2.2.1 Derivation of Drag Coefficient

In the current experiments, it was not possible to make pressure measurements in the wake of the test model. Only velocity measurements were possible with the LDV system, which makes local velocity measurements at the intersection of two crossed laser beams. Because the test section of the water tunnel was cylindrical, the LDV was only able to measure points lying on the horizontal transverse plane that bisected the test section through the sides. This limitation was imposed by the requirement that the each laser beam must have the same incidence angle when entering the cylindrical test section. Since a full velocity field cannot be measured with the cylindrical test section, the flow was necessarily assumed to be axially symmetric. Because of these limitations, it was necessary to derive a formula for the drag coefficient of an axisymmetric body that only made use of velocity measurements to compute the drag coefficient. The following derivation closely follows the procedure used by Dimotakis [2] for a Cartesian coordinate system and a nominally two-dimensional flow.

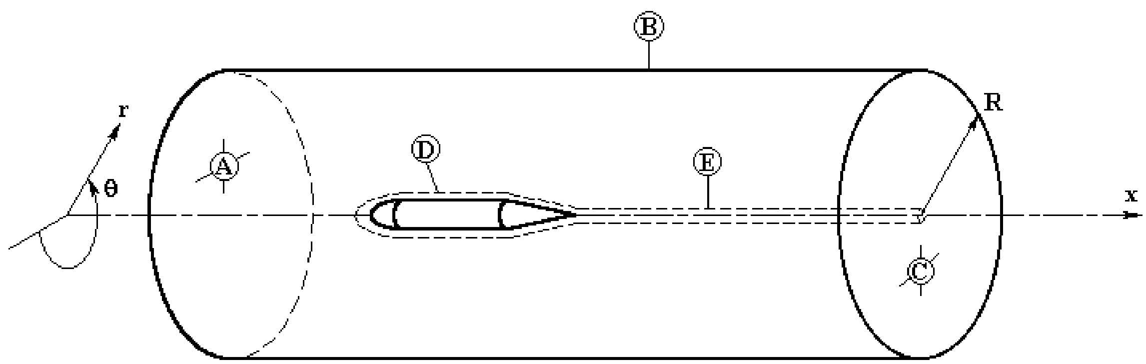

Figure 2.1: Control volume representation.

Consider an axisymmetric body located along the x-axis. The body is surrounded by a cylindrical volume $\mathcal{V}$ along the x-axis whose surfaces are ABCDE, as shown in Figure 2.1. Surface A is the transverse plane upstream of the submerged body, where uniform freestream conditions are assumed to apply. Surface B is a streamtube surrounding the submerged body; surface C is the transverse plane downstream of the body; surface D is the fluid surface adjacent to the body; and surface E is a cylindrical surface of infinitesimally small diameter extending along the x-axis from surface D to surface C.

The Navier-Stokes equations are

$$div \ \underset{\sim}{u} = 0 \, , \tag{2.11}$$

and

$$\frac{\partial}{\partial t}\underset{\sim}{u} + \nabla \cdot \underset{\sim}{u}\underset{\sim}{u} + \frac{1}{\rho}\left(\nabla p - \nabla \cdot \underset{\approx}{\tau}\right) = 0 \, , \tag{2.12}$$

where $\underset{\sim}{u}$ is the velocity vector, ρ is the fluid density, p is the pressure, and $\underset{\approx}{\tau}$ is the viscous stress tensor. Integrating the momentum equation with respect to the interior volume $\mathcal{V}$ and applying Gauss' theorem, this becomes

$$\frac{\partial}{\partial t}\int_{\mathcal{V}} \underset{\sim}{u} \, d\mathcal{V} + \int_S \underset{\sim}{u}\underset{\sim}{u} \cdot d\underset{\sim}{S} + \frac{1}{\rho}\int_S \left(p - p_\infty \right) d\underset{\sim}{S} - \frac{1}{\rho}\int_S \underset{\approx}{\tau} \cdot d\underset{\sim}{S} = 0 \, , \tag{2.13}$$

where $d\underset{\sim}{S}$ is a vector directed along the outward surface normal, of magnitude equal to the surface element *dS*; and the freestream pressure p_∞ is chosen as the origin in pressure. The various operators and vectors in equation (2.13) are defined in cylindrical coordinates:

Gradient operator
$$\nabla \equiv \hat{e}_x \frac{\partial}{\partial x} + \frac{\hat{e}_\theta}{r}\frac{\partial}{\partial \theta} + \hat{e}_r \frac{\partial}{\partial r} \tag{2.14}$$

Velocity vector
$$\underset{\sim}{u} = \hat{e}_x u + \hat{e}_\theta v + \hat{e}_r w \tag{2.15}$$

Surface element vector
$$d\underset{\sim}{S} = \hat{e}_x dS_x + \hat{e}_\theta dS_\theta + \hat{e}_r dS_r \tag{2.16}$$

The surface element magnitudes are further defined:

$$dS_x = r d\theta dr\,; \tag{2.17}$$

$$dS_\theta = dr dx\,; \tag{2.18}$$

$$dS_r = r d\theta dx\,. \tag{2.19}$$

The viscous stress tensor $\underset{\approx}{\tau}$ is defined for incompressible flow as

$$\underset{\approx}{\tau} = \mu\left[\nabla \underset{\sim}{u} + \left(\nabla \underset{\sim}{u}\right)^T\right], \tag{2.20}$$

where μ is the absolute viscosity. When $\underset{\approx}{\tau}$ is expanded in cylindrical coordinates, it is written as:

$$\begin{aligned}\underset{\approx}{\tau} = \mu\Bigg\{ & 2\frac{\partial w}{\partial r}\hat{e}_r\hat{e}_r + \left(\frac{1}{r}\frac{\partial w}{\partial \theta} + \frac{\partial v}{\partial r}\right)\hat{e}_r\hat{e}_\theta + \left(\frac{\partial w}{\partial x} + \frac{\partial u}{\partial r}\right)\hat{e}_r\hat{e}_x + \left(\frac{\partial v}{\partial r} + \frac{1}{r}\frac{\partial w}{\partial \theta}\right)\hat{e}_\theta\hat{e}_r + \\ & + \left(\frac{2}{r}\frac{\partial v}{\partial \theta}\right)\hat{e}_\theta\hat{e}_\theta + \left(\frac{\partial v}{\partial x} + \frac{1}{r}\frac{\partial u}{\partial \theta}\right)\hat{e}_\theta\hat{e}_x + \left(\frac{\partial u}{\partial r} + \frac{\partial w}{\partial x}\right)\hat{e}_x\hat{e}_r + \\ & + \left(\frac{1}{r}\frac{\partial u}{\partial \theta} + \frac{\partial v}{\partial x}\right)\hat{e}_x\hat{e}_\theta + 2\frac{\partial u}{\partial x}\hat{e}_x\hat{e}_x\Bigg\}\end{aligned} \tag{2.21}$$

When the cylindrical coordinate operators and vectors are substituted into equation (2.13) and dotted with $\hat{e}_x$, the x-component of the momentum equation is obtained:

$$\begin{aligned}& \frac{\partial}{\partial t}\int_{\forall} u\,d\forall + \int_S uw\,dS_r + \int_S uv\,dS_\theta + \int_S uu\,dS_x + \frac{1}{\rho}\int_S \left(p - p_\infty\right) dS_x + \\ & -\nu\int_S\left(\frac{\partial u}{\partial r} + \frac{\partial w}{\partial x}\right)dS_r - \nu\int_S\left(\frac{1}{r}\frac{\partial u}{\partial \theta} + \frac{\partial v}{\partial x}\right)dS_\theta - \nu\int_S\left(2\frac{\partial u}{\partial x}\right)dS_x = 0\end{aligned} \tag{2.22}$$

Taking the time average of the equation eliminates the time derivative term:

$$\int_S \overline{uw}\,dS_r + \int_S \overline{uv}\,dS_\theta + \int_S \overline{uu}\,dS_x + \frac{1}{\rho}\int_S (\overline{p} - p_\infty)\,dS_x - \nu\int_S \left(\frac{\overline{\partial u}}{\partial r} + \frac{\overline{\partial w}}{\partial x}\right) dS_r + \\ -\nu\int_S \left(\frac{1}{r}\frac{\overline{\partial u}}{\partial \theta} + \frac{\overline{\partial v}}{\partial x}\right) dS_\theta - \nu\int_S \left(2\frac{\overline{\partial u}}{\partial x}\right) dS_x = 0\ . \tag{2.23}$$

At this point it is helpful to decompose each surface integral to the sum of the integrals over each sub-surface A, B, C, D, E; i.e.,

$$\int_S = \int_A + \int_B + \int_C + \int_D + \int_E\ . \tag{2.24}$$

The integrals over surface E are zero because surface E has been chosen to be a streamtube of infinitesimally small diameter across which there is no flux. The integral over surface D represents the drag force per unit mass per unit volume that the fluid control volume $\mathcal{V}$ exerts on the body in the x-direction. The resulting equation is:

$$\frac{D}{\rho} = -\int_B \overline{uw}\,R\,d\theta\,dx - \left\{\int_A + \int_C\right\}\overline{u^2}\,r\,d\theta\,dr - \frac{1}{\rho}\left\{\int_A + \int_C\right\}(\overline{p} - p_\infty)\,r\,d\theta\,dr + \\ +\nu\int_B \left(\frac{\partial\overline{u}}{\partial r} + \frac{\partial\overline{w}}{\partial x}\right) R\,d\theta\,dx + 2\nu\left\{\int_A + \int_C\right\}\frac{\partial\overline{u}}{\partial x}\,r\,d\theta\,dr\ , \tag{2.25}$$

where R is the radius of the cylindrical control volume. If the maximum body diameter d is the characteristic length of the submerged body, and equation (2.25) is divided by $\frac{1}{2}U_\infty^2\frac{\pi}{4}d^2$, then:

$$\frac{D}{\frac{1}{2}\rho U_\infty^2 \frac{\pi}{4} d^2} = \frac{-8}{\pi d^2 U_\infty^2} \int_B \overline{uw} R d\theta dx - \frac{8}{\pi d^2 U_\infty^2} \left\{ \int_A + \int_C \right\} \overline{u^2} r d\theta dr +$$
$$- \frac{1}{\frac{1}{2}\rho U_\infty^2 \frac{\pi}{4} d^2} \left\{ \int_A + \int_C \right\} (\overline{p} - p_\infty) r d\theta dr + \tag{2.26}$$
$$+ \frac{8\nu}{\pi d^2 U_\infty^2} \int_B \left(\frac{\partial \overline{u}}{\partial r} + \frac{\partial \overline{w}}{\partial x} \right) R d\theta dx + \frac{16\nu}{\pi d^2 U_\infty^2} \left\{ \int_A + \int_C \right\} \frac{\partial \overline{u}}{\partial x} r d\theta dr \, .$$

The drag coefficient of the body is defined as

$$C_D = \frac{D}{\frac{1}{2}\rho U_\infty^2 \frac{\pi}{4} d^2} \, , \tag{2.27}$$

and the time averaged pressure coefficient $\overline{c}_p$ is defined as

$$\overline{c}_p = \frac{\overline{p} - p_\infty}{\frac{1}{2}\rho U_\infty^2} \, . \tag{2.28}$$

Applying these definitions, equation (2.26) becomes:

$$C_D = \frac{-8}{\pi d^2} \int_B \frac{\overline{uw}}{U_\infty^2} R d\theta dx - \frac{8}{\pi d^2} \left\{ \int_A + \int_C \right\} \frac{\overline{u^2}}{U_\infty^2} r d\theta dr - \frac{4}{\pi d^2} \left\{ \int_A + \int_C \right\} \overline{c}_p r d\theta dr +$$
$$+ \frac{8\nu}{\pi d^2 U_\infty^2} \int_B \left(\frac{\partial \overline{u}}{\partial r} + \frac{\partial \overline{w}}{\partial x} \right) R d\theta dx + \frac{16\nu}{\pi d^2 U_\infty^2} \left\{ \int_A + \int_C \right\} \frac{\partial \overline{u}}{\partial x} r d\theta dr \, . \tag{2.29}$$

Equation (2.11) is integrated over the control volume $\cancel{V}$, and Gauss' Theorem is applied to obtain:

$$\int_{\cancel{V}} \nabla \cdot \underset{\sim}{u} \, d\cancel{V} = \int_S \underset{\sim}{u} \cdot d\underset{\sim}{S} = 0 \, . \tag{2.30}$$

Expanding equation (2.30) and multiplying by a factor of $\dfrac{8}{\pi d^2 U_\infty}$, the continuity equation is written in terms of integrals over the sub-surfaces A, B, and C:

$$\frac{8}{\pi d^2 U_\infty}\left\{\int_A + \int_C\right\}\bar{u} r d\theta dr + \frac{8}{\pi d^2 U_\infty}\int_B \bar{w} R d\theta dx = 0 \qquad (2.31)$$

Equation (2.31) can be subtracted from the C_D equation (2.29):

$$\begin{aligned} C_D = & \frac{-8}{\pi d^2}\int_B \frac{\overline{uw} - U_\infty \bar{w}}{U_\infty^2} R d\theta dx - \frac{8}{\pi d^2}\left\{\int_A + \int_C\right\}\frac{\overline{u^2} - U_\infty \bar{u}}{U_\infty^2} r d\theta dr + \\ & -\frac{4}{\pi d^2}\left\{\int_A + \int_C\right\}\bar{c}_p r d\theta dr + \frac{8\nu}{\pi d^2 U_\infty^2}\int_B \left(\frac{\partial \bar{u}}{\partial r} + \frac{\partial \bar{w}}{\partial x}\right) R d\theta dx + \\ & + \frac{16\nu}{\pi d^2 U_\infty^2}\left\{\int_A + \int_C\right\}\frac{\partial \bar{u}}{\partial x} r d\theta dr \ . \end{aligned} \qquad (2.32)$$

Surface A has been chosen to be far enough upstream of the body such that the velocity and pressure are assumed to be uniform across the surface and equal to the freestream values U_∞ and p_∞, respectively. Thus the second and third terms of equation (2.32) are equal to zero on surface A.

The velocity components *u* and *w* can be separated into a mean value and a fluctuating part, i.e.:

$$u = \bar{u} + u' ; \qquad (2.33)$$

$$w = \bar{w} + w' ; \qquad (2.34)$$

$$\overline{u^2} = \bar{u}^2 + \overline{u'^2} ; \qquad (2.35)$$

$$\overline{uw} = \bar{u}\bar{w} + \overline{u'w'} . \qquad (2.36)$$

The product $\overline{uw}$ appears only in the integrals over surface B. Surface B has been defined to be a streamtube that lies outside of the regions where disturbances from the wall or the body are assumed negligible, which implies

$$\overline{w} = \overline{u'w'} = \frac{\partial \overline{w}}{\partial x} = 0 \tag{2.37}$$

on surface B.

Applying the conditions on surfaces A and B, and assuming that the surfaces are far enough away from the body that all mean velocity gradients are negligible, equation (2.32) is reduced to:

$$\begin{aligned} C_D = {} & \frac{8}{\pi d^2}\left\{\int_C\right\}\frac{\overline{u}}{U_\infty}\left(1-\frac{\overline{u}}{U_\infty}\right) r\,d\theta\,dr - \frac{8}{\pi d^2}\left\{\int_C\right\}\frac{\overline{u'^2}}{U_\infty^2} r\,d\theta\,dr + \\ & -\frac{4}{\pi d^2}\left\{\int_C\right\}\overline{c}_p r\,d\theta\,dr \ . \end{aligned} \tag{2.38}$$

Now define the displacement thickness δ_1 at the downstream surface C such that

$$\left(\pi R^2 - \pi \delta_1^{\ 2}\right) U_0 \equiv \int_C \overline{u} r\,d\theta\,dr\,; \tag{2.39}$$

$$\delta_1^{\ 2} = \frac{1}{\pi}\int_C \left(1-\frac{\overline{u}}{U_0}\right) r\,d\theta\,dr\,; \tag{2.40}$$

where U_0 is defined as the velocity outside of the wake at surface C. Since there is no mass flux through surface B, the flow rate through surfaces A and C must be equal:

$$\pi R^2 U_\infty = \left(\pi R^2 - \pi \delta_1^{\ 2}\right) U_0 \,. \tag{2.41}$$

Equation (2.41) can be rearranged to the form:

$$\frac{U_0}{U_\infty} = \frac{1}{1-\left(\dfrac{\delta_1}{R}\right)^2} \,. \tag{2.42}$$

The effects of freestream acceleration due to displacement thickness δ_1 on the pressure coefficient can be separated from the pressure differences across the wake by dividing the pressure coefficient into two separate components:

$$\bar{c}_p = \frac{\bar{p} - p_\infty}{\frac{1}{2}\rho U_\infty^2} = \frac{p_0 - p_\infty}{\frac{1}{2}\rho U_\infty^2} + \frac{\bar{p} - p_0}{\frac{1}{2}\rho U_\infty^2} = c_{p_0} + \bar{c}_{p_w}\,, \tag{2.43}$$

where c_{p_0} is the pressure coefficient of the flow outside of the wake, and $\bar{c}_{p_w}$ is the time-averaged pressure coefficient of the flow within the wake. Bernoulli's equation can be applied outside of the wake between surfaces A and C:

$$p_0 + \frac{1}{2}\rho U_0^2 = p_\infty + \frac{1}{2}\rho U_\infty^2\,. \tag{2.44}$$

Using equation (2.42) with equation (2.44), c_{p_0} can be defined in terms of the displacement thickness:

$$c_{p_0} = -\left(\frac{\delta_1}{R}\right)^2 \frac{2 - \left(\frac{\delta_1}{R}\right)^2}{\left[1 - \left(\frac{\delta_1}{R}\right)^2\right]^2}\,. \tag{2.45}$$

Using equations (2.45), (2.40), and (2.42) in equation (2.38), the equation for the drag coefficient becomes:

$$\begin{aligned} C_D = & \frac{8}{\pi d^2 \left[1 - \left(\delta_1/R\right)^2\right]^2} \left\{ \int_C \frac{\bar{u}}{U_0}\left(1 - \frac{\bar{u}}{U_0}\right) r\,d\theta\,dr - \int_C \frac{\overline{u'^2}}{U_0^2}\, r\,d\theta\,dr - \frac{\pi \delta_1^4}{2 d^2 R^2} \right\} + \\ & + \frac{4}{\pi d^2} \int_C \bar{c}_{p_w}\, r\,d\theta\,dr\,. \end{aligned} \tag{2.46}$$

2.2.2 Self-Preserving Flow

The generation of a wake behind a body is an example of a developing flow. The velocity deficit of the wake is greater and the width of the wake is smaller near the body, but as the flow moves downstream the velocity deficit decreases and the wake width increases as the wake turbulence dies out. An assumption of self-preserving flow stipulates that the transverse velocity profiles retain the same functional forms at points further downstream of the body, but that the length scales and mean flow property values scale according to the distance downstream of the body. According to Townsend [3], the definition of a self preserving flow is one in which the variation of a mean value quantity *M* in the flow direction must be of the form:

$$M = M_1 + m_0(x)\, func\left(r / l_0(x)\right), \tag{2.47}$$

where the length scale l_0 and the scale of quantity m_0 are functions of *x*, and M_1 is the reference mean value.

Assume $\bar{u}$, $\overline{u'^2}$, and $\bar{p}$ have the forms:

$$\bar{u}(r) = U_0 - u_0(x) f(r / l_0(x)); \tag{2.48}$$

$$\overline{u'^2} = u_0^2(x) g(r / l_0(x)); \tag{2.49}$$

$$\bar{p} = p_0 + \frac{1}{2}\rho u_0^2(x) \Pi(r / l_0(x)). \tag{2.50}$$

Introduce the non-dimensional coordinate η:

$$\eta = \frac{r}{l_0(x)}. \tag{2.51}$$

Then,

$$\bar{u}(r) = U_0 - u_0(x) f(\eta), \tag{2.52}$$

$$\overline{u'^2} = u_0^2(x) g(\eta), \text{ and} \tag{2.53}$$

$$\bar{p} = p_0 + \frac{1}{2}\rho u_0^2(x)\Pi(\eta). \tag{2.54}$$

Applying these forms to equation (2.40) and integrating in θ results in the displacement thickness in terms of the length and velocity scales, and an integration of the function $f(\eta)$:

$$\delta_1^2 = 2\frac{u_0(x) l_0^2(x)}{U_0} \int_0^{R/l_0} f(\eta)\eta d\eta. \tag{2.55}$$

Now consider the time averaged pressure coefficient of the wake $\bar{c}_{p_w}$:

$$\bar{c}_{p_w} = \frac{\bar{p} - p_0}{\frac{1}{2}\rho U_\infty^2}. \tag{2.56}$$

Substituting the equations (2.42) and (2.54) into equation (2.56) yields

$$\bar{c}_{p_w} = \frac{1}{\left[1-\left(\delta_1/R\right)^2\right]^2} \frac{u_0^2(x)}{U_0^{\ 2}} \Pi(\eta). \tag{2.57}$$

When the functional forms of equations (2.51) through (2.55), and equation (2.57) are applied to the drag coefficient equation (2.46), the resulting equation is:

$$C_D = \frac{8}{\pi d^2}\left\{\int_C l_0^2 \eta d\eta d\theta - \int_C \frac{u_0 l_0^2}{U_0} f(\eta)\eta d\eta d\theta - \frac{2\pi}{R^2}\frac{u_0{}^2 l_0^4}{U_0{}^2}\left(\int_0^{R/l_0} f(\eta)\eta d\eta\right) + \right.$$
$$- \int_C \left(1 - 2\frac{u_0}{U_0} f(\eta) + \frac{u_0^2}{U_0{}^2} f^2(\eta)\right) l_0^2 \eta d\eta d\theta - \pi \frac{u_0^2 l_0^2}{U_0{}^2}\int_0^{R/l_0} \Pi(\eta)\eta d\eta + \tag{2.58}$$
$$\left. - \frac{u_0^2 l_0^2}{U_0{}^2}\int_C g(\eta)^2 \right\}\left[1 - \frac{2}{R^2}\frac{u_0 l_0^2}{U_0}\int_0^{R/l_0} f(\eta)\eta d\eta\right]^{-2},$$

where u_0 and l_0 are implicitly functions of x.

White [4] states that the velocity defect of a circular wake can be expressed as a Gaussian distribution. The function $f(\eta)$ is assumed to have the Gaussian form:

$$f(\eta) = e^{-(\ln 2)\eta^2} . \tag{2.59}$$

The presence of the (ln 2) factor in the exponent of equation (2.59) references the length scale to the wake half width b, which is defined as the width of the wake where the velocity deficit is half of the maximum velocity deficit. Substitution for $f(\eta)$ in equation (2.58) and integration results in:

$$C_D = \frac{16}{d^2}\left\{\frac{u_0 l_0^2}{2U_0(\ln 2)} - \frac{u_0^2 l_0^2}{4U_0{}^2(\ln 2)} + \frac{u_0^2 l_0^4}{4R^2 U_0{}^2(\ln 2)^2} + \right.$$
$$\left. - \frac{u_0^2 l_0^2}{U_0{}^2}\int_C g(\eta)\eta d\eta - \frac{u_0^2 l_0^2}{2U_0{}^2}\int_0^{R/l_0} \Pi(\eta)\eta d\eta\right\}\left[1 - \frac{u_0 l_0^2}{R^2 U_0(\ln 2)}\right]^{-2} . \tag{2.60}$$

According to White [4], the self-similarity parameters u_0 and l_0 of a circular wake with small velocity defect are described by the power law relations $u_0 \propto x^{-2/3}$ and $l_0 \propto x^{1/3}$. A further fit is introduced such that

$$\frac{u_0}{U_0} = c_u\left(\frac{x - x_0}{d}\right)^{-2/3}, \text{ and} \tag{2.61}$$

$$\frac{l_0}{d} = c_l \left(\frac{x - x_0}{d} \right)^{1/3}, \tag{2.62}$$

where x_0 is the origin from the curve fitting process. The drag coefficient equation becomes:

$$\begin{aligned} C_D = 16\left[1 - \frac{c_u c_l^{\,2}}{(\ln 2)}\left(\frac{d}{R}\right)^2\right]^{-2} & \left\{ \frac{c_u c_l^{\,2}}{2(\ln 2)}\left[1 + \frac{c_u c_l^{\,2}}{2(\ln 2)}\left(\frac{d}{R}\right)^2\right] + \right. \\ & \left. - c_u^{\,2} c_l^{\,2}\left(\frac{x - x_0}{d}\right)^{-2/3}\left[\frac{1}{4(\ln 2)} + \int_C g(\eta)\eta d\eta - \frac{1}{2}\int_0^{R/l_0} \Pi(\eta)\eta d\eta\right]\right\}. \end{aligned} \tag{2.63}$$

By extrapolating far enough downstream, the terms containing $\left(\frac{x - x_0}{d}\right)^{-2/3}$ vanish, and the equation for drag coefficient becomes:

$$C_D = 16\left[1 - \frac{c_u c_l^{\,2}}{(\ln 2)}\left(\frac{d}{R}\right)^2\right]^{-2} \left\{ \frac{c_u c_l^{\,2}}{2(\ln 2)}\left[1 + \frac{c_u c_l^{\,2}}{2(\ln 2)}\left(\frac{d}{R}\right)^2\right]\right\}. \tag{2.64}$$

If it is assumed that the body diameter d is much less than the control volume radius R, the terms containing $(d/R)^2$ may be neglected, and the equation for C_D reduces to

$$C_D \cong \frac{8 c_u c_l^{\,2}}{(\ln 2)}. \tag{2.65}$$

CHAPTER III

EXPERIMENTAL APPARATUS

3.1 Water Tunnel

3.1.1 Water Tunnel History and Description

The Aerospace Engineering Department Water Tunnel is located in Patterson Engineering Laboratories on the Mississippi State University main campus. A layout drawing of the water tunnel is shown in Figure 3.1. The preliminary design of the water tunnel was begun in 1961 by Dr. Graham Wells [5]. The tunnel was constructed from fiberglass by Aerospace Engineering Department shop technicians, with the largest section diameter being 40 inches, the limit of shop capabilities. The test section is a 4-ft length of 11-inch inner diameter Plexiglas® tube. This results in a contraction ratio of 13.22:1. The length of the contraction is 5 feet, and the contraction was designed for minimal adverse pressure gradient and a uniform exit velocity profile. The original drive system was a Buick V-8 automotive engine with belt drive, but this was later changed to an electric motor retaining the old belt drive, and finally to an efficient direct-drive electric motor. The drive section is located on the first floor of Patterson Laboratory, and the test section is located on the second floor. The current motor has a remote control panel so that the tunnel can be operated from the second floor. The 3-bladed propeller

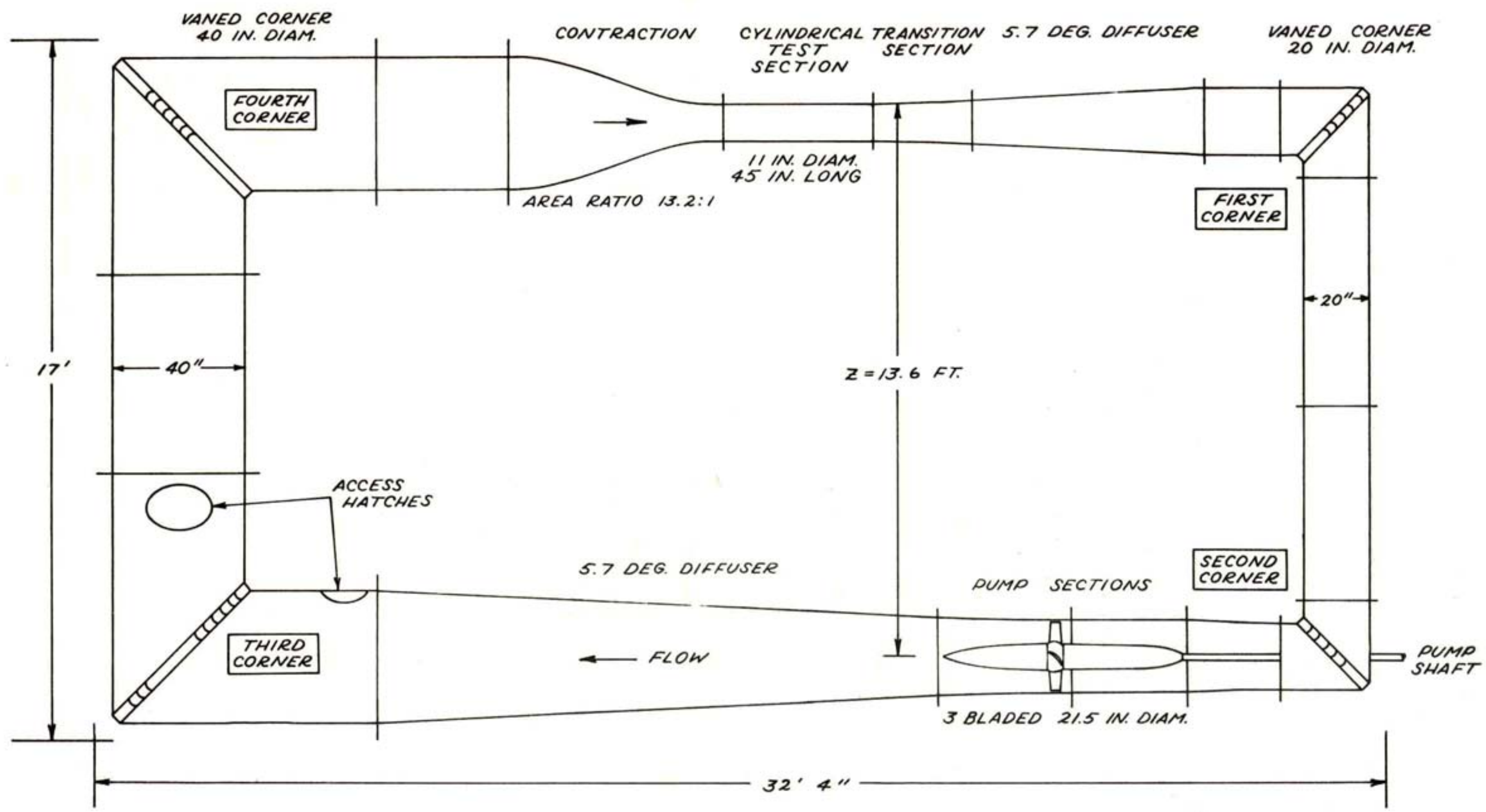

Figure 3.1: Diagram of MSU water tunnel (from Wells [5]).

was reportedly taken from a Second World War amphibious assault vehicle. The water fill line is located on the second floor. The valve to this water line is opened to pressurize the water tunnel to the line pressure, which is usually about 50 psig. The tunnel pressurization and the hydrostatic head suppress cavitation from occurring in the tunnel drive section. The tunnel contains no flow straighteners, but does have turning vanes on each of the corners. Another set of tunnel segments consisting of contraction, test section, and diffuser were built to study nominally two-dimensional flows, but these sections were never fitted into the tunnel and are in storage.

The primary motivation for the construction of the water tunnel at MSU was to attract hydrodynamic research from the submarine and shipbuilding industries, which were booming in the 1950's and 1960's as the modern nuclear submarine was being developed. The facility never saw any of this research, and for most of the 1980's and the 1990's the tunnel was not operated nor maintained. It was renovated in the late 1990's to support research at the new U.S. Navy Large Cavitation Channel (LCC) in Memphis, Tennessee. The first experiments performed after the renovation studied the effect of tap hole size on static pressure measurements in the test section [6]. During these experiments a number of problems developed with the tunnel that required further work, and the tunnel was taken apart.

3.1.2 Repainting of Corners, Turning Vanes, and Drive Section

At the end of the previous testing on the water tunnel, it was noticed that certain things had to be repaired. Although the entire tunnel interior had received a new finish of four coats of Duratec® vinyl ester, the finish on the tunnel corners, turning vanes, and drive section had peeled off. It was necessary to recoat these corner sections to protect the fiberglass structure from water penetration. Additional coats of Interlux InterProtect® epoxy paint were applied to the tunnel drive section and the third corner downstream of the test section. InterProtect® is formulated to prevent water penetration into fiberglass boat hulls.

3.1.3 Drive Bearing Modifications

A more serious problem that developed during the previous testing of the tunnel was bearing overheating and burnout. The water-cooled Cutless bearing inside the drive section of the tunnel was completely burned out. When the drive section was disassembled, it was discovered that the step of the drive shaft had been cut into by the edge of the brass Cutless bearing. It was determined that the location of the shaft had shifted downstream relative to the support bearings, causing the step to butt against the brass Cutless bearing. This not only cut off the water flow through the bearing, but damaged the stainless steel shaft as well. To ensure adequate water flow, a Little Giant® 1/40 hp water pump was placed into the bearing cooling water feed line. Previously, water was forced through the feed line by the differential pressure between the third corner (where the water is picked up) and the drive section.

It was also noted that a hydraulic press was needed to press the Cutless bearing into and out of its stainless steel holder. Measurement of the holder inner diameter and the Cutless bearing outer diameter showed that the holder diameter was 0.015 inch too small, and out of round. It was speculated that local buckling of the bearing as it was pressed into the holder caused the inner diameter to shrink enough to cause the bearing to grip the drive shaft too tightly. A new bearing slipped onto the shaft easily, but after being pressed into the bearing holder it could only be forced onto the shaft. It was decided to bore out the bearing holder to a diameter that was 0.002 inch less than the bearing outer diameter. The parts were prepared for installation by placing the bearing in a freezer and by heating the bearing holder in an oven. The chilled bearing was quickly inserted into the heated holder. Afterwards, as the temperatures equalized, the bearing expanded and the holder shrinked, providing a solid grip on the bearing.

Other modifications were made to the bearing to ensure adequate water flow. First, the bearing length was reduced by 0.4 inch to fit completely within the holder sleeve. Previously, the bearing had protruded from the holder end and had severely restricted the flow into the holder from the feed line outlets on either side of the holder end. Another minor modification to the bearing was the filing of ramps into the brass and rubber, to aid the water flow into the rubber/shaft interface. Furthermore, the drive shaft steps in this region were moved back 0.875 inch to insure no further contact with the bearing end.

Later, during tunnel assembly, it was finally determined why the drive shaft had drifted downstream and caused the Cutless bearings to fail. During the last renovation and upgrade of the tunnel, a new 50 hp electric motor was installed. Power was directly transmitted to the shaft by means of a flexible connection. It was discovered during tunnel assembly that the previous power train lacked a reverse thrust bearing. The power system before that had a belt drive system that incorporated a reverse thrust bearing. A thrust bearing and locking collar were fitted onto the shaft so that the new thrust bearing worked against the existing outer bearing casing. This prevented the shaft from shifting longitudinally when reverse thrust was applied. Although the motor was not run in reverse, reverse thrust was applied when the tunnel was slowed or stopped, causing the propeller to work against the water flow. It was speculated that in the previous power train, the shaft was pulled downstream just enough to bind the shaft step against the Cutless bearing during these transitional phases of operation.

3.1.4 Other Tunnel Modifications

Several other modifications were made to the tunnel to improve tunnel installation and maintenance. A new and larger drain line was placed into the bottom of the third corner. A Culligan® HF-150 water filter rated at 125 psi was fitted into the fill line of the water tunnel. Culligan® S1A 20-micron sediment water filter cartridges were used to filter out the great amounts of rust and sediment in the fill line, providing cleaner water in the tunnel. To further aid in keeping the tunnel clean, common pool algaecide was added to the tunnel to prevent organic pollution. Ball valves were added onto the percolator domes, which are installed on each corner of the water tunnel to collect air that is pressurized out of solution with the water during operation. Algaecide and seeding particles can be added to the filled water tunnel by use of the funnel on the percolator on the first corner.

The bearing bolts that hold the bearing holder in the drive section of the tunnel were modified. Previously, these bolts were very short and difficult to reach. Also, the bolt had to pass through three separately threaded lugs. All but the bearing holder lug holes were stripped of their threads. 5/16 x 3-1/8 inch Allen head bolts were then used to secure the holder. The extra length of these new bolts extended the bolt head to the outside of the drive fairing, which greatly simplified the assembly of the tunnel drive section. These bolts had to be custom made from 3/8 x 3-1/8 inch bolts. The ends of these bolts were turned down on a lathe to 5/16-inch diameter and threaded.

3.1.5 Propeller Knocking

After final assembly of the tunnel and initial run-up, a loud knocking noise was heard in the propeller area. Because the clearance between the propeller and the wall is less than a paper thickness, the most likely source of the noise was the propeller striking the wall. After running the tunnel unpressurized for some time, the noise was reduced at the higher normal operating pressures. It was speculated that the propeller had worn itself in during the unpressurized run. The reduced noise was deemed acceptable, and was ignored during further testing.

3.2 Laser Doppler Velocimeter

The laser Doppler velocimeter (LDV), which is also called a laser Doppler anemometer (LDA), employs the Doppler theory to measure particle velocities at a point in a fluid flow. The measurement probe of the system is a lens that focuses two laser beams of the same wavelength onto a point determined by the focal length of the probe lens. The intersection of the two beams forms an ellipsoid-shaped measurement volume where a distinct pattern of light is formed. The amplitudes of the two laser beams add together to form alternating regions of high amplitude and low amplitude light—this is called the fringe pattern. If a light-reflecting particle were to pass through this measurement volume in a direction normal to the fringe pattern, it would reflect pulses of light as it passes through the high amplitude fringes of the measurement volume. The wavelength and the angle of intersection of the beams are known, which determines the distance between each fringe in the measurement volume. The LDV system thus measures the time interval between reflected bursts of light, and is able to calculate the particles speed through the measurement volume in the direction normal to the fringe pattern.

The above description assumes that the frequencies of the two beams are the same, and are in “sync”. This is achieved by optically splitting a single laser beam. However, it is undesirable to have both beams of the same frequency. If the frequency of one of the beams is shifted by a slight amount, the fringe pattern “scrolls” in one direction. This allows the LDV system to discern between negative and positive velocity directions. The LDV system does this through the use of a Bragg cell. The Bragg cell is a device that shifts one of the laser beams frequencies by directing the beam through a prism that is electro-mechanically vibrated at the desired frequency shift.

The laboratory LDV is a Dantec FiberFlow system. The laser source is a Spectra Physics Stabilite 2017 Argon-ion laser. This unit consists of a laser, a laser power supply, and a remote control module. The laser and the power supply run on 220 V and require water-cooling. The output beam of this system is directed into the FiberFlow transmitter, which contains the beam splitter and Bragg cell. The beam splitter splits the primary laser beam into up to three pairs of beams. The three pairs of beams may be 476.5 nm wavelength (violet), 488 nm (blue), or 514.5 nm (green). One pair of beams represents one velocity component that can be measured. Currently, the optics are not installed on the violet beams, rendering the system capable of only two-component measurements. The Bragg cell puts a 40-Mhz frequency shift into one of the beams of each pair. The laser beams are then transmitted to a 2-D probe by means of fiber optic cables. The probe has a 80 mm diameter lens with a focal length of 800 mm. The probe is equipped with a 1.95 ratio beam expander. The system is computer-controlled and the data are collected and processed using the Dantec Flow Velocity Analyzer (FVA) and its associated software.

3.3 LDV Calibration Apparatus

3.3.1 Calibration Apparatus Description

The LDV was calibrated by measuring the tangential velocity at a point of radius *r* on a disk with a rough surface rotating at a precisely controlled angular velocity. The disk was rough-cut from a sheet of 0.25-inch Plexiglas and was turned down on a lathe to a radius of 12 inches. An aluminum hub was attached to the backside of the disk by two screws. The disk assembly was not balanced, nor was the disk perfectly flat; the disk wobbled ±0.381 mm perpendicular to the disk plane near the extreme radius. The wobble should not have affected the accuracy of the calibration measurements, but rather it just moved the disk surface back and forth in the axial direction through the measurement volume, which had a dimension of 4.303 mm. A rough disk surface was created by attaching a 12-inch diameter, 80-grit sandpaper disk with a spray-adhesive such as 3M

Super77®. This rough surface simulated a particle flow for the LDV system to measure. A pinhole was located in the center of the disk for laser alignment purposes.

The calibration disk was rotated by a Compumotor SM233BE-NTQN type servo motor. The motor was mounted onto aluminum T-stock, which was then clamped onto the lower water tunnel test section tie bars with four “c”-clamps. These tie bars were located just beneath the test section. This location allowed an LDV calibration to be performed without physically moving the traverse system out of alignment with the water tunnel. It was necessary to shim the motor mount 2.25 inches above the lower support bars in order to place the center of the disk within the vertical limits of the LDV traverse. The TQ10X Servo Controller was mounted on an aluminum beam, which acted as a heat sink and allowed the unit to hang from the lower tie bars.

3.3.2 Uncertainty of Disk Radius Measurement

The first task in the calibration process was to locate the LDV measurement volume on the center of the calibration disk. The current laboratory arrangement did not allow the LDV measurement volume to measure more than a few centimeters below the calibration disk center, so an alignment procedure was developed using only the top half of the disk surface. First, the LDV measurement volume was visually centered by positioning the probe so that the measurement volume “disappeared” into the pinhole on the calibration disk center. The centering accuracy of this visual method was only ±1.0 mm. A more accurate centering alignment was achieved by using the LDV beam system and the traverse to measure the disk radius, and to center the traverse by measuring off of the top and sides of the calibration disk.

Designate the left side of the disk as x_1, and the right side as x_2. The radius R of the disk is then:

$$R = \frac{x_2 - x_1}{2}. \tag{3.1}$$

After the LDV measurement volume was visually centered as closely as possible, the blue beams were used to measure the radius of the disk at x_1 and x_2.

According to the methods advocated by Coleman and Steele [7], the uncertainty of the disk radius is given by the following equation:

$$U_R^2 = \left(\frac{\partial R}{\partial x_1}\right)^2 P_{x_1}^2 + \left(\frac{\partial R}{\partial x_2}\right)^2 P_{x_2}^2 + \left(\frac{\partial R}{\partial x_1}\right)^2 B_{x_1}^2 + \left(\frac{\partial R}{\partial x_2}\right)^2 B_{x_2}^2 + 2\left(\frac{\partial R}{\partial x_1}\right)\left(\frac{\partial R}{\partial x_2}\right) B_{x_1 x_2}, \tag{3.2}$$

where P_{x_k} denotes the random uncertainty associated with x_k, B_{x_k} denotes the systematic uncertainty associated with x_k, and $B_{x_1 x_2}$ denotes the correlated systematic uncertainties of the variables x_1 and x_2. Because the same procedure was used to measure both x_1 and x_2, the same random and systematic uncertainties were applied to each x-coordinate.

Only one source of random uncertainty was found in the procedure, and that was the judgment of the operator as to the exact alignment of the beams onto the edge of the disk. The possible error in this alignment was estimated to be half of a beam diameter, or ±0.675 mm. Possible random uncertainty of the traverse was considered negligible, as the traverse specification reported a resolution of 6.25 μm.

There were a number of systematic uncertainty sources. One systematic uncertainty source was the specified accuracy of the traverse, which was ±0.2 mm. Another systematic uncertainty was in the radius of the Plexiglas® disk itself. Using a dial indicator, a variation in disk radius of ±0.3429 mm was measured. The total systematic uncertainty of the location of x_1 and x_2 then was ±0.3967 mm.

Because the measurement of x_1 and x_2 was by the same method, the systematic uncertainties of these two variables were completely correlated. The correlated systematic error term is

$$B_{x_1 x_2} = B_{x_1} B_{x_2} \, . \tag{3.3}$$

Using these uncertainty estimates, the uncertainty in the measurement of disk radius R was ±0.4773 mm. The actual measured value of the calibration disk radius using this procedure was 152.9875 mm, or 6.023 inches.

3.3.3 Uncertainty in Radial Positioning During Calibration

All random and systematic uncertainties of the radial measurement used in the calibration procedure were associated with the centering of the measurement volume in the y-direction (vertical). This was done by visually locating the green laser beams on the top edge of the calibration disk, which introduced a random error of ±0.675 mm, as discussed previously. The measurement volume was then moved down a distance equal to the disk radius, which introduced a systematic error of ±0.4773 mm. Accounting for the additional systematic error introduced by the traverse accuracy (±0.2 mm) and the finite diameter of the measurement volume (±0.0995 mm), the total systematic uncertainty in the radial position measurement was ±0.5270 mm. Because the traverse was able to resolve to within 6.25 μm of a given position, and the step sizes during the calibration tests were on the order of millimeters, the total random uncertainty in the radial position measurement was ±0.675 mm.

3.3.4 Positioning the Measurement Volume in *z*

Before proceeding with the calibration, the measurement volume must be located such that its center is bisected by the surface of the calibration disk. After the measurement volume was centered in x and y, the volume was moved to a point close to the center of the disk, but not in the pinhole. With the calibration disk rotating, the z position was adjusted to maximize the LDV data rate. This was done by enabling the high voltage in the FVA software and connecting an oscilloscope to the appropriate channel on the FVA. The z position was then adjusted to maximize the signal-to-noise ratio as was seen on the oscilloscope. To further improve the calibration data, the high voltage settings were adjusted to increase the signal-to-noise ratio, again using the oscilloscope as a guide. It was found that a high voltage setting of 800-900 worked well for this purpose.

3.3.5 Uncertainty in Angular Velocity Measurement

The angular velocity of the servo motor was precisely controlled and reported to the computer control software every few seconds. A stroboscopic tachometer was used to verify the accuracy of the rotational velocity at low and high speeds. There was no discrepancy between the angular velocity reported by the motor controller and the velocity measured by the tachometer. The systematic uncertainty of the rotational velocity was set at the resolution limits of the stroboscopic tachometer, which was ±0.05 rad/s.

During the actual calibration measurements, data were only taken when the motor controller reported a stable reading of the target speed. However, at some speeds (especially lower speeds) a random fluctuation of disk speed was noticed in the digital readout of the motor control program. This flicker was on the order of 0.03 rev/s. Thus the random uncertainty for the disk speed was estimated to be ± 0.03 rev/s, or ±0.18 rad/s.

3.3.6 Random Uncertainty of LDV Velocity Measurement

The random uncertainty of the mean velocities measured by the LDV was determined to be ±0.004 m/s. This estimate was developed by taking 25 measurements of a reference speed, and determining the standard deviation of the mean velocities of these measurements. The random uncertainty of an LDV mean velocity measurement is twice the standard deviation. These measurements were done for several reference velocities, as shown in Figure 3.2.

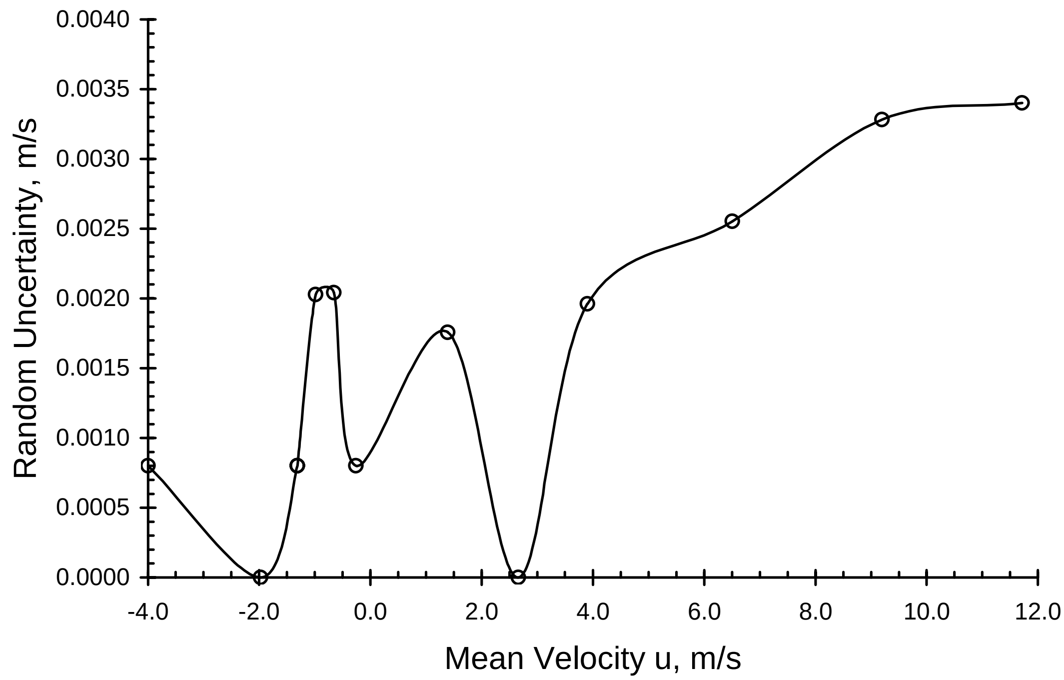

Figure 3.2: Random uncertainties of LDV mean velocity measurements.

3.3.7 Calibration Results

Several calibration tests were made. In one type of test, the measurement volume was placed at a specific radius and the disk angular velocity was stepped through a range of speeds. In a second type of test, the disk angular velocity was set to a specific speed and the measurement volume was moved through a range of radii using the traverse. Care was taken during these procedures to not overload the LDV system's photo multiplier tubes (PMT). As a guideline, FVA software high voltage settings of 800-900 worked well, with a low laser current such as 10 Amps.

The results for the series of four calibration tests from 1/25/02 are shown below. The method of constant angular velocity was used for these tests because it could be executed quickly. The angular velocity was set at 15 revolutions per second to avoid velocity fluctuations. Tangential velocities were measured in a range of radii from –5 mm to 127 mm. These combinations of radius and angular velocity enveloped the range of expected velocities in the water tunnel, and included small negative velocities. The radii positions were stepped sequentially up and down, to detect any possible hysteresis. No hysteresis was detected in the measurements, and the results were very consistent.

The comprehensive data set consisted of 140 points. A linear regression was applied to the data to return a slope of $m = 0.9681$ and an intercept of $b = -0.0352$ m/s. An uncertainty analysis was performed analytically on the regression equation, and a second order curve fit was applied to the uncertainty to obtain an estimate of the regression uncertainty $U_{u\text{-}regress}$ for new values of calibrated velocity u_c:

$$u_c = 0.9681 u_{FVA} - 0.0352 \tag{3.4}$$

$$U_{u-regress} = 0.0507 + (-2.4825 \times 10^{-4}) u_c + (2.4639 \times 10^{-5}) u_c^{\,2} \tag{3.5}$$

The linear regression with uncertainty bands is plotted in Figure 3.3 for the entire calibration range. The linear regression plot is repeated in Figure 3.4 for the range of expected water tunnel velocities. This second plot also includes the calibration data points with error bars.

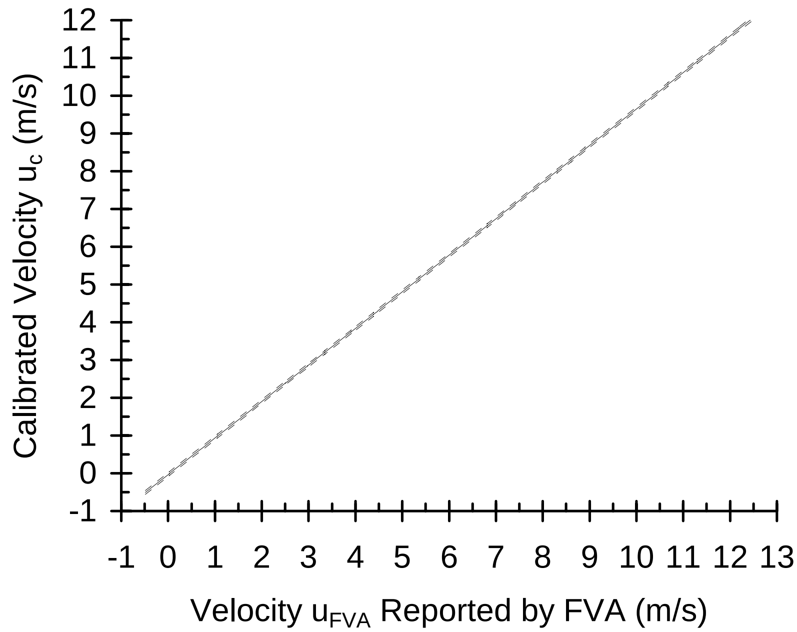

Figure 3.3: LDV calibration plot with upper and lower uncertainty bands.

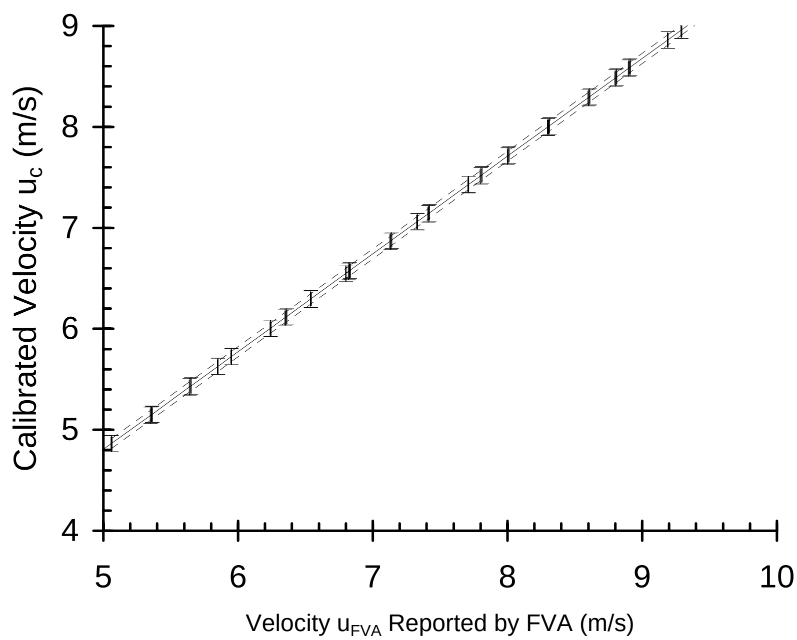

Figure 3.4: Calibration plot of expected water tunnel test speed range, with uncertainty bands and error bars on the data points.

3.4 Submarine Model and Mount

The submarine shape that was tested was identical to one that was used in a number of experiments at the LCC. The submarine hull shape is plotted in Figure 3.5. The model constructed for the current experiment was 286.47 mm (11.278 in) long with a diameter of 25.4 mm (1 in), which resulted in a fineness ratio of 11.278. The hull form had no appendages or fins, but did incorporate a propeller hub shape on the end. The model was constructed of two pieces of stainless steel bar stock. The hull shape was turned down on a CNC lathe in the MSU Mechanical Engineering shop. The two pieces were screwed together to form the complete single model.

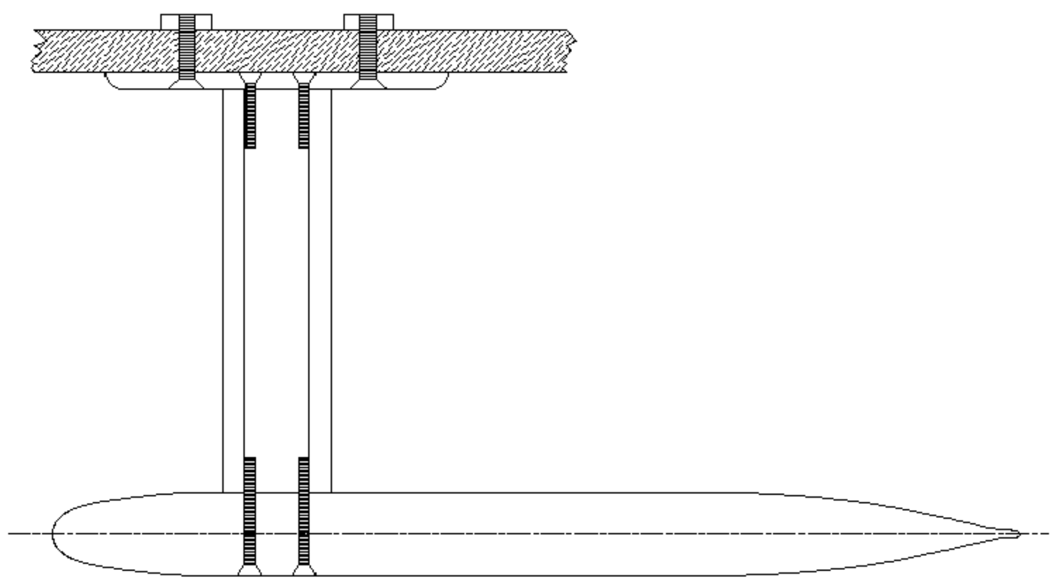

Figure 3.5: Submarine model drawing showing mounting details.

The model was mounted along the test section centerline by means of a single stainless steel strut. The strut was 1.25 inches wide and 0.125 inches thick, which was just wide enough for 4-40 size threads. Two 4-40 size flat head screws were used to mount the model on one end of the strut. Two more 4-40 size flat head screws were used to mount the other end of the strut onto a stainless steel mounting plate. This mounting plate was in turn mounted onto the inside of the test section wall by two flat head 10-32 screws, which were threaded into two holes in the test section wall. Nuts were put on the outside to further secure the mount. Silicon was used between the mounting plate and the test section wall to prevent water leakage. Also, all exposed countersunk screw heads in the mounting plate and in the model were filled with epoxy and sanded flush with 400-grit sandpaper. The model was mounted so that the nose of the submarine was approximately 6 body diameters (6 inches) downstream of the test section entrance. The strut was mounted on the submarine model in the position corresponding approximately to the position of the strut on the LCC submarine model. The leading edge of the strut was located at x/L_{sub} = 0.183.

CHAPTER IV

EXPERIMENTAL PROCEDURE AND RESULTS

4.1 LDV Configuration

4.1.1. LDV Alignment with Water Tunnel

The lightweight traverse that was used with the LDV had three axes at right angles. The x-direction was chosen to be the direction of flow; the y-direction was the vertical axis transverse to the direction of flow, and the z-direction was the horizontal axis transverse to the direction of flow. The first alignment was to position the traverse system so that the x-axis of the traverse was parallel to the centerline of the water tunnel. This was achieved by hanging plumb lines over the side of the test section and taping a length of string on the floor between the two points. A second length of string was then taped onto the floor so that it was parallel to the first string, with about 20 inches of distance between them. The traverse was then positioned so that plumb lines that were hung from the traverse were lined up on the second string. Next, the probe was aligned on the horizontal plane of the test section centerline. To do this, the green beams were first centered on the outside wall of the test section in the vertical direction (y-direction) by positioning the entering laser beams and the exiting reflected beams in a straight, horizontal line at a point near the middle of the test section. This adjustment was made by moving the probe with the traverse. The probe was then traversed in the x-direction to the end of the test section. At this new position, the beams were adjusted in the y-direction by raising or lowering the traverse platform on that end, if it was necessary. This procedure accounted for any angular displacement the water tunnel may have had from the true horizontal.

The origin of the experiment coordinates was a point on the centerline of the outside test section wall and 7.5 body diameters downstream of the submarine body propeller hub. For the x-direction reference, the blue beams were touched to the aft end of the hub; the traverse was then moved downstream 7.5 body diameters, which was a distance of 190.5 mm. A piece of masking tape with a small black dot was placed at this point, so that when the measurement volume was on the origin, the laser beam "disappeared" when viewed through the laser safety goggles.

To center the measurement volume onto the outside wall in the z-direction, the following procedure was used. First the z-position was adjusted until the laser beams formed a fine point on the test section wall. The traverse coordinates were then set to zero. A refinement was necessary to insure that the middle of the measurement volume was on the outer wall surface. Using the green beams, the measurement volume was stepped in increments of 0.5 mm in the z-direction, starting from a point a short distance off the wall. The anode current reading in the LDV software output was recorded at each point. The point where the highest anode current was recorded was the point where the center of the measurement volume was on the outer surface of the wall. The data rate was a maximum at this point.

It was found that this alignment procedure had to be performed for every new experiment because the water tunnel shifted position under operation. The masking tape with the black dot aided in locating the x datum easily. The y and z datum had to be reconfirmed using the procedures outlined above.

4.1.2 Laser Beam Refraction Correction

The refraction of the laser beams when changing media must be accounted for when positioning the measurement volume within the test section. Fortunately, the index of refraction for water and Plexiglas® are nearly the same, so that only one refraction index needed to be considered. The overall effect of the change in media from air to water was that the ratio of the travel distance of the probe volume within the test section to the travel distance of the probe traverse outside of the test section was equal to the index of refraction of the new medium. The index of refraction for water is 4/3.

4.2 Test Section Flow Characteristics

A number of velocity measurements were made of the water tunnel test section with no model to determine the flow characteristics of the water tunnel. Three positions were selected for velocity profile measurements: $x/L = 0.125$, $x/L = 0.492$, $x/L = 0.738$; where L is the length of the test section. At each of these positions, several velocity profiles were recorded for three different motor input speeds. For $x/L = 0.492$, the motor input speeds were 500, 550, and 600 rpm. It was noted during this time that the water tunnel was being excited near its natural frequency at motor input speeds that were multiples of 200 rpm. The water tunnel shook very badly at 600 rpm, so that for the velocity profiles at x/L = 0.125 and x/L = 0.738, the motor input speeds were 500, 550, and 630 rpm.

The water was seeded with 5-micron silicon carbide during these tests to increase data rates. A laser current of 16 Amps was used throughout the tests. The PMT high voltage setting had to be increased as the probe measurement volume was moved further into the test section. Table 4.1 below lists the optimum high voltage setting for a given range of z for a moderately seeded flow.

Table 4.1: PMT high voltage settings for test section regions.

Range in z (mm)	**PMT High Voltage**
15-40	700
45-75	800
80-100	1000
105-120	1200

The plots of the water tunnel velocity profiles are shown below in Figure 4.1 through Figure 4.4 for each of the motor speeds. The presence of the wall boundary layer is noted on the right hand side of each plot. It is evident that the tunnel speeds are more consistent at higher velocities and near the entrance to the test section. At x/L = 0.125, all velocity profiles fall right on top of each other, even with the distinctive kinks in the profile. These kinks and shifts can be seen in other profiles as well. Figure 4.5 shows the representative velocity profile kinks and shifts for x/L = 0.492 and a motor input speed of 500 rpm.

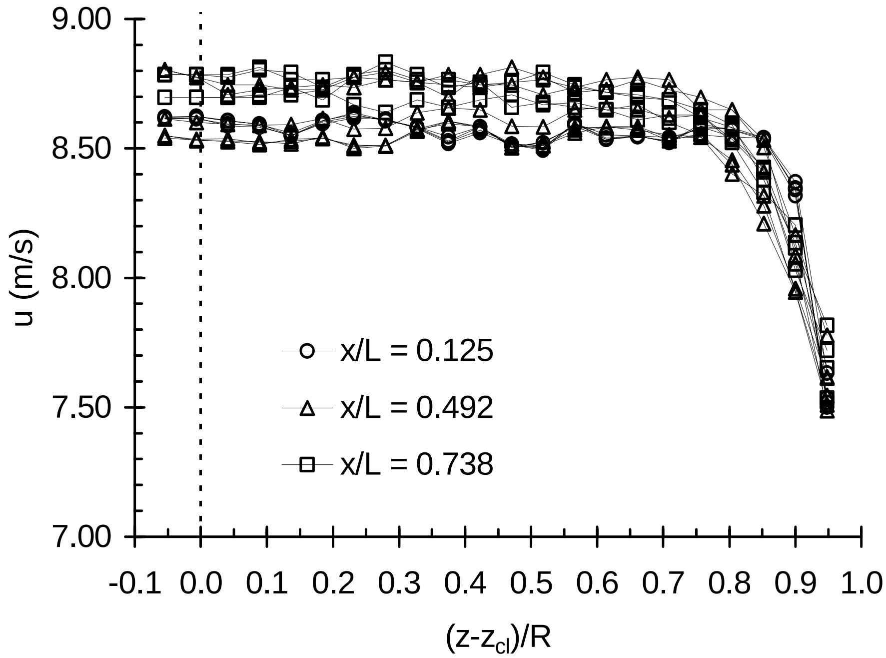

Figure 4.1: Velocity profiles in the test section at motor input speed of 500 rpm.

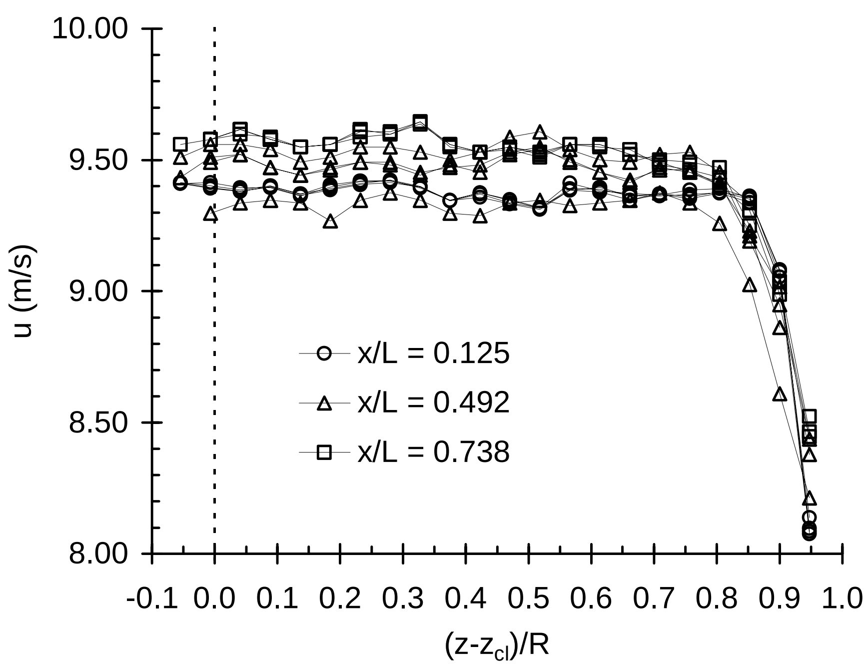

Figure 4.2: Velocity profiles in the test section at motor input speed of 550 rpm.

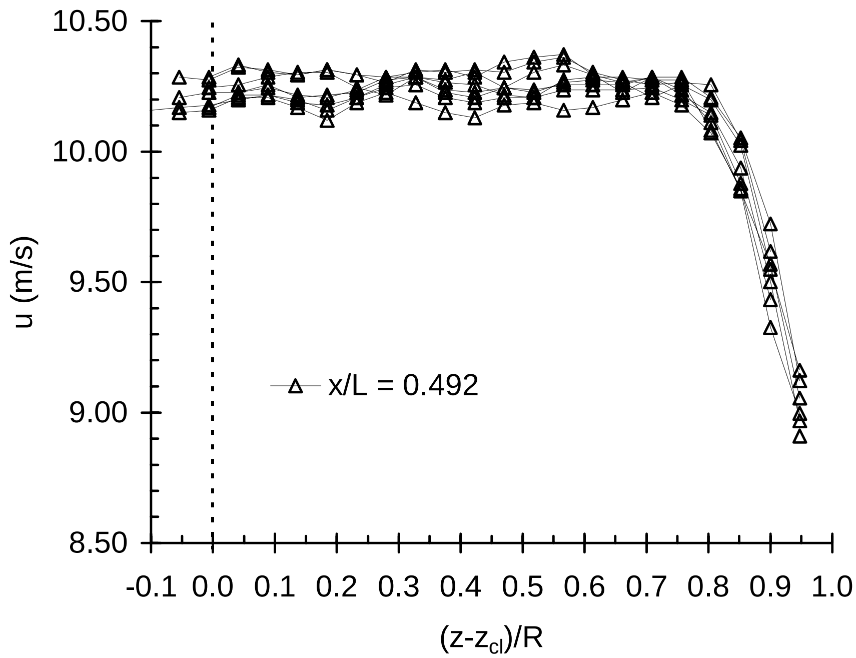

Figure 4.3: Velocity profiles of the water tunnel at motor input speed of 600 rpm.

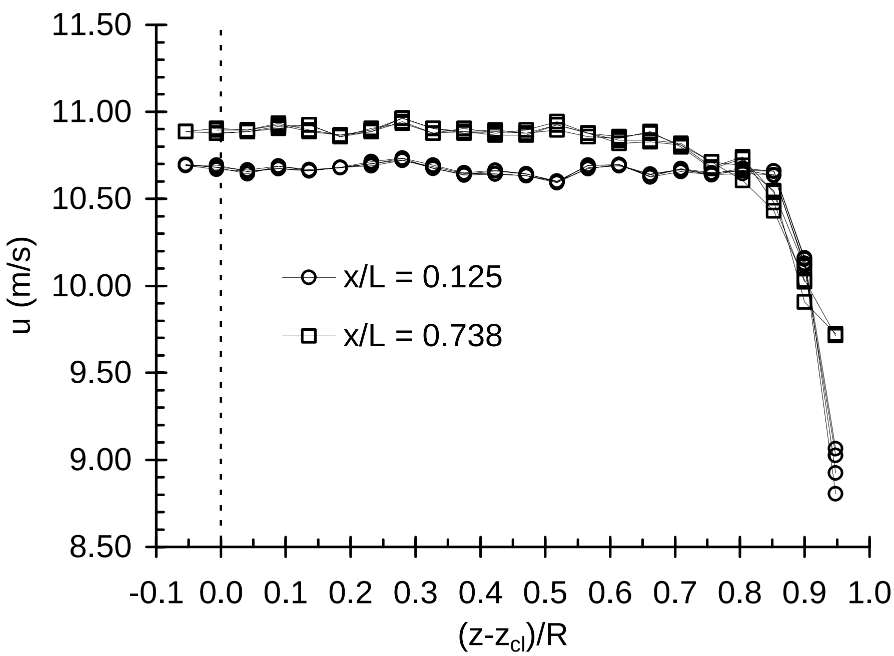

Figure 4.4: Velocity profiles of the water tunnel at motor input speed of 630 rpm.

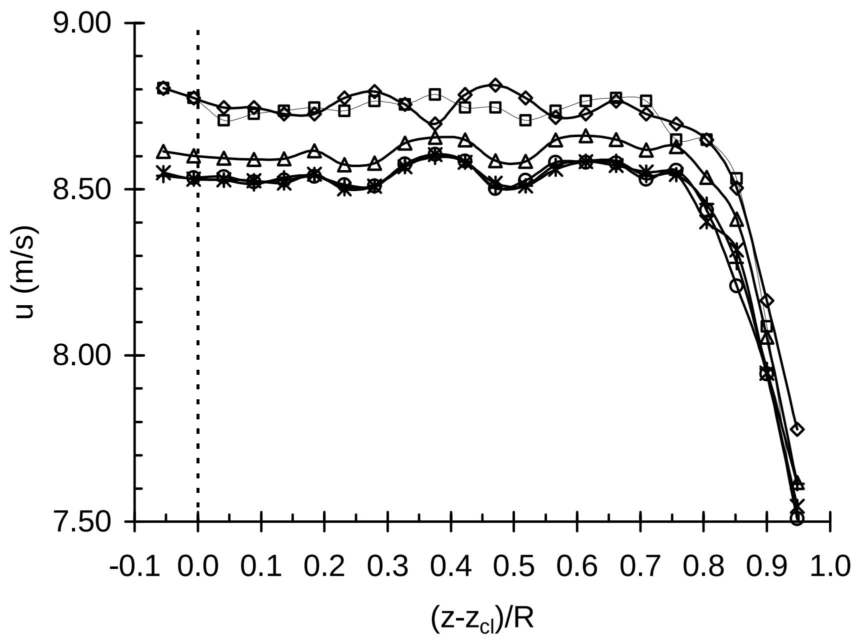

Figure 4.5: Velocity profiles taken at *x/L* = 0.492, 500 rpm, showing typical velocity shift and non-uniform profile.

During the initial testing of the LDV system on the water tunnel, numerous measurements were taken at a fixed point within the test section to determine the optimal LDV system configuration settings. During this time the motor was set to a constant speed. It was observed that the mean velocity would occasionally shift up or down by approximately 0.5 m/s. After several occurrences of this phenomenon, it was noted that the shifts seemed to occur suddenly after an approximate 20-minute period. No motor speed fluctuations were noted in the motor controller feedback. Several long period tests were performed to try to capture the exact period of the velocity shift, but these proved inconclusive. Besides being a physical phenomenon of the tunnel, the velocity shift could have been caused by a faulty LDV Bragg cell that was only working intermittently.

The kinks in the velocity profiles that were repeatable from data set to data set, even when the velocity shift occurs, were most likely caused by the local differences in the optical properties of the test section wall. As the measurement volume was moved across the test section, the actual area of the wall that the beams passed through changed. The repeatability of these kinks at the same r/R positions indicates that the local optical properties of the test section were affecting the crossing angle or the location of the beam intersection that formed the measurement volume. The standard deviation from the local mean velocities was found to be no more than 0.06 m/s at any point in the test section, which amounted to a systematic uncertainty estimate of ±0.12 m/s in velocity measurement due to the optical properties of the test section.

Figures 4.6, 4.7, and 4.8 show the local turbulence intensity factor u_{rms}/u at x/L = 0.492 and motor input speeds of 500, 550, and 600 rpm. The typical value for the freestream turbulence intensity is 1.5 %, which is slightly higher than is desirable. Figures 4.9, 4.10, and 4.11 illustrate the typical uncertainty associated with the velocity profile measurements. Figure 4.12 plots the same data as Figure 4.11, but the velocity axis has been expanded to full scale to give a better sense of the relative magnitudes of the error. The error in the velocity measurements includes the fossilized systematic error from the calibration, the systematic uncertainty estimate due to the test section optics, and the random uncertainty of each of the point measurements. The radial position errors are due to uncertainties in the traverse calibration, the finite length of the measurement volume, and the uncertainty in the test section radius R.

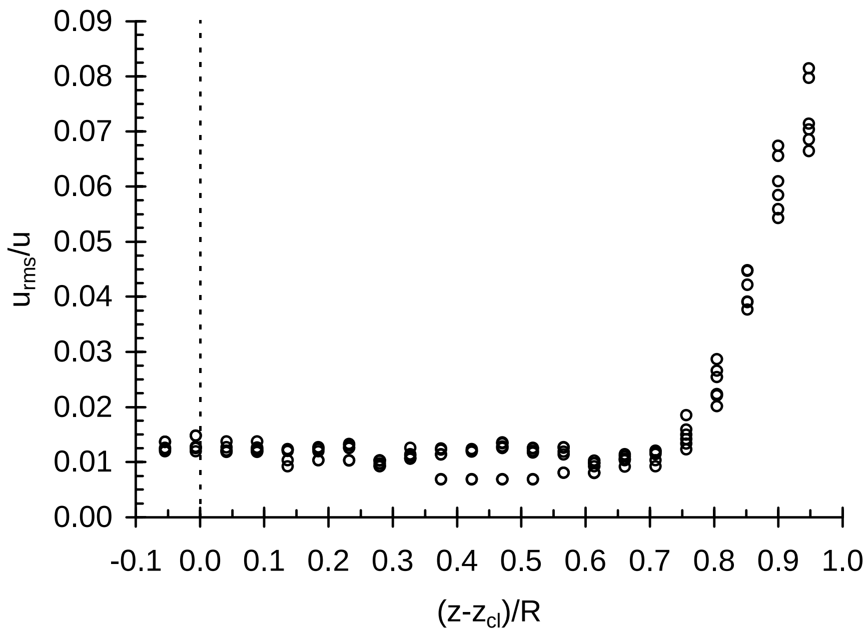

Figure 4.6: Local turbulence intensity factors at *x/L* = 0.492, 500 rpm.

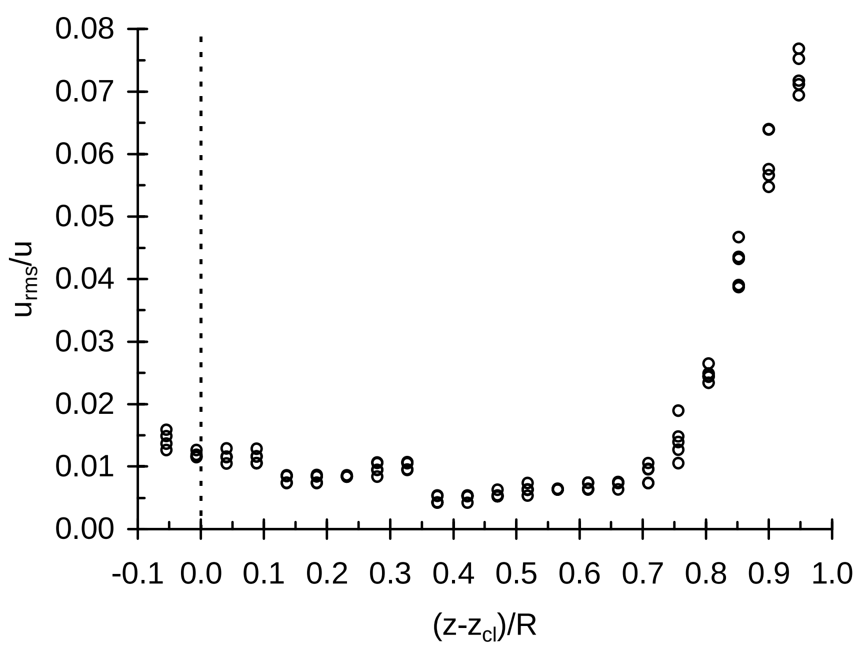

Figure 4.7: Local turbulence intensity factors at *x/L* = 0.492, 550 rpm.

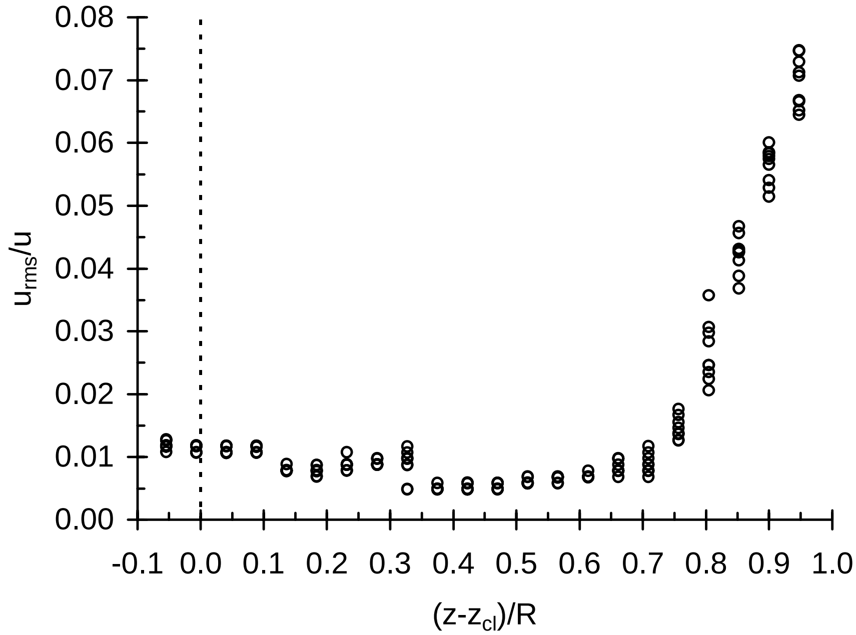

Figure 4.8: Local turbulence intensity factors at *x/L* = 0.492, 600 rpm.

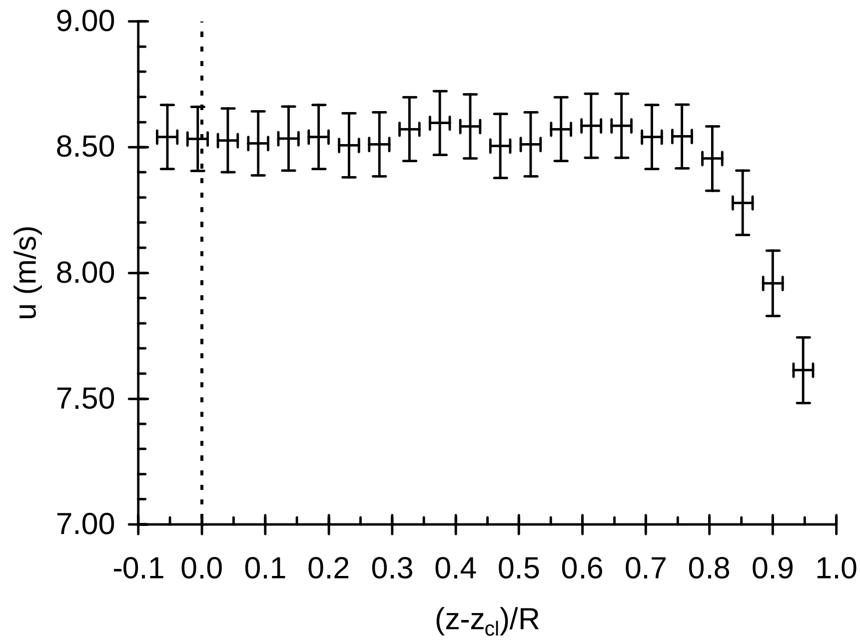

Figure 4.9: Typical velocity profile with error bars, *x/L* = 0.492, 500 rpm.

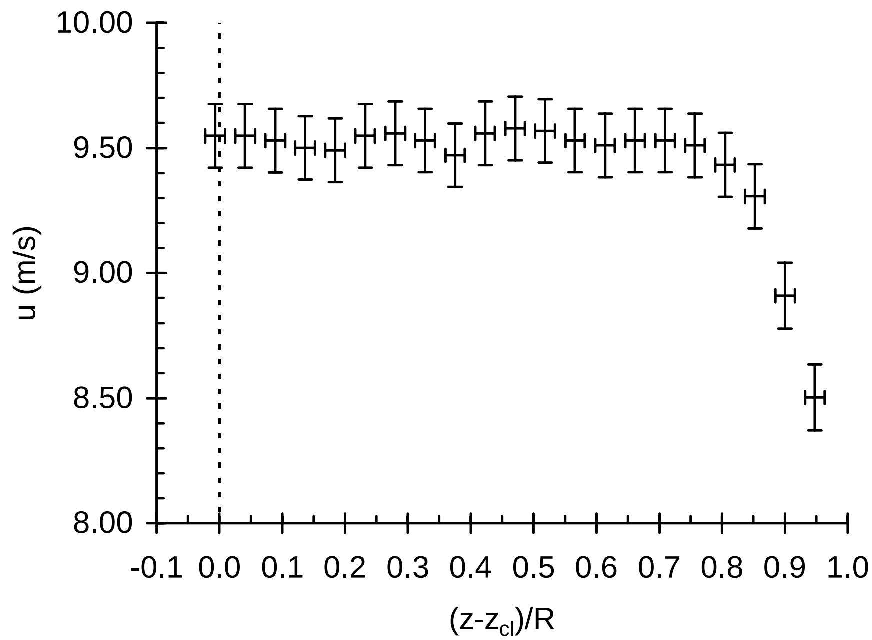

Figure 4.10: Typical velocity profile with error bars, *x/L* = 0.492, 550 rpm.

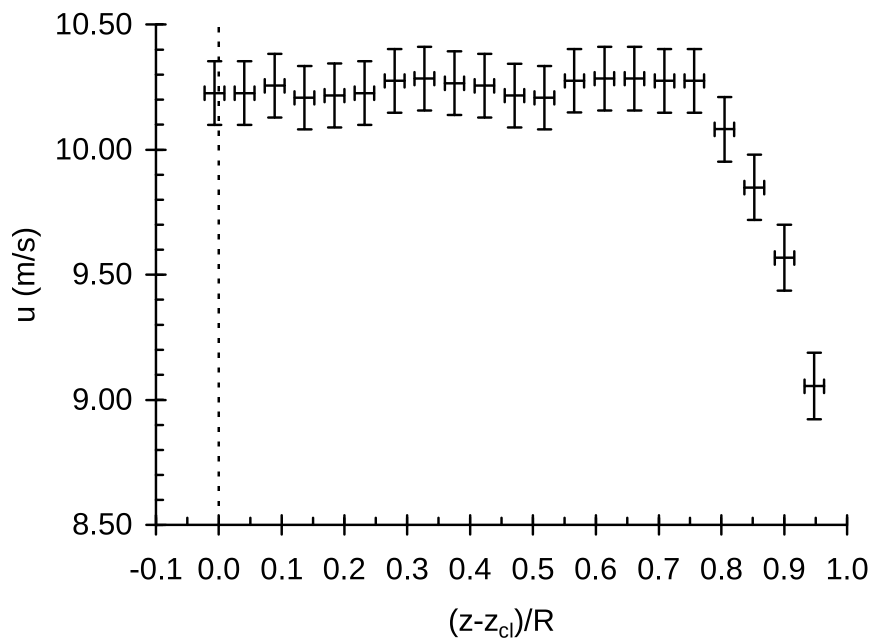

Figure 4.11: Typical velocity profile with error bars, *x/L* = 0.492, 600 rpm.

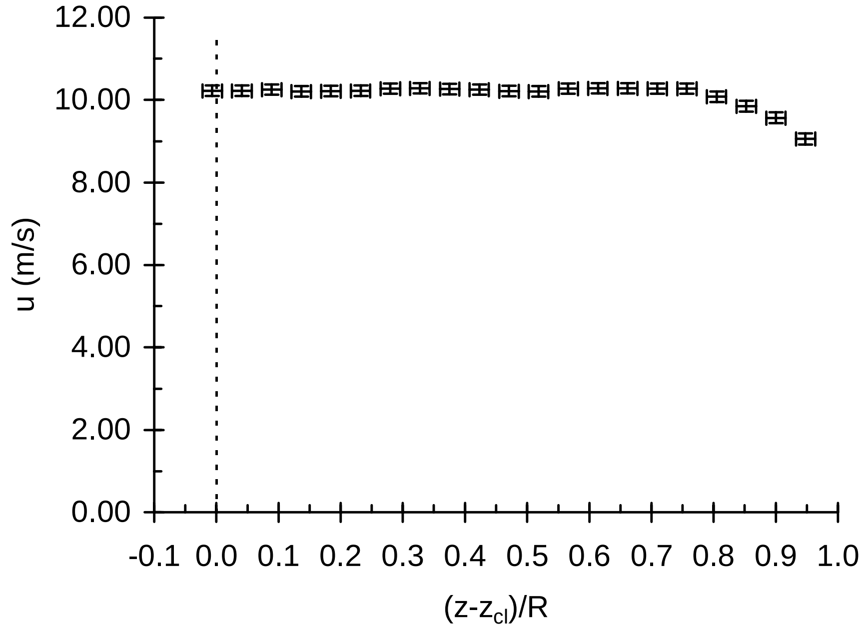

Figure 4.12: Typical velocity profile with error bars, *x/L* = 0.492, 600 rpm, repeated with full velocity scale to show relative magnitude of errors.

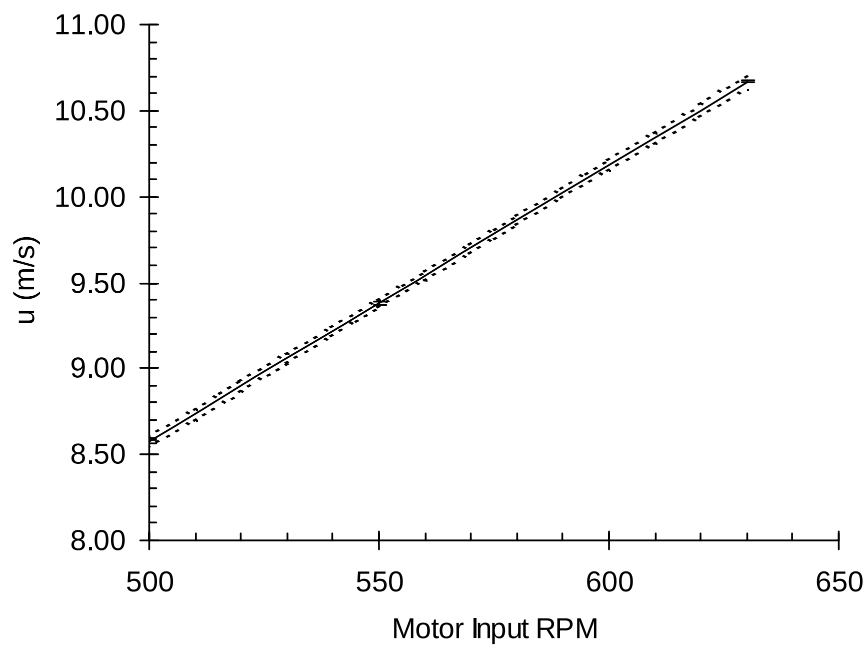

Figure 4.13: Mean test section velocity at *x/L* = 0.125 versus motor input speed. Error bars are shown on the data points, and uncertainty bands are shown around the curve fit.

Figure 4.13 demonstrates the linear relationship between motor input speed and test section velocity as measured at *x/L* = 0.125. The error bars are shown on the three data points at 500, 550, and 630 rpm. The uncertainty bands that are shown apply to the curve fit, and are derived from the "classical approach" to regression uncertainty as described in Coleman and Steele [7]. A least squares linear regression to this data is given by the equation:

$$U_\infty = 0.0161\,\Omega + 0.5241\,, \tag{4.1}$$

where Ω is the motor input speed in revolutions per minute and U_∞ denotes the test section velocity at *x/L* = 0.125. The uncertainty associated with the regression is given by the equation:

$$U_{U_\infty - regress} = 0.040878\left[\frac{1}{3}+\frac{(\Omega-560)^2}{8600}\right]^{1/2}. \tag{4.2}$$

The uncertainty of U_∞ from the curve fit could be reduced by a factor of six by taking velocity profiles at nine different motor speeds rather than just using three motor speeds.

4.3 Submarine Model Wake Experiments

For the submarine wake measurements, the tunnel motor speed was set to 500 rpm. Velocity profiles were taken at several *x/d* stations behind the model, where *x/d* = 0 is the end of the model. Velocity profiles were measured at *x/d* = 10, 13, 16, 19, 22, 25, and 28. The time required to complete one complete set of profiles was approximately 5 hours. Most of that time was spent measuring the wake velocity deficits, which had accompanying low data rates. Optimum LDV settings for the wake profile measurements were found through trial and error. The laser current setting for the tests was 16 Amps. The PMT high voltage setting was 1050, with no seeding in the tunnel. A drape was used over the test section and traverse to block light noise from the overhead lights. A dark drape was also hung vertically behind the test section to reduce glare off of the wall.

The wake velocity profiles and the turbulence intensity factors from the five days of testing are shown in Figure 4.14 through Figure 4.23. The point spacing for the 5/16/02 through 5/22/02 data was 3.33 mm, which corresponded to a traverse movement of 2.5 mm. For the remaining days, the point spacing was reduced to 2 mm (corresponding to a traverse movement of 1.5 mm) and the measurement of the velocity profile at x/d = 28 was discontinued. The point spacing was reduced to increase the number of points in the wake. The effect of measurement volume overlap was ignored. The measurements at x/d = 28 were discontinued for an operational time savings of nearly half an hour.

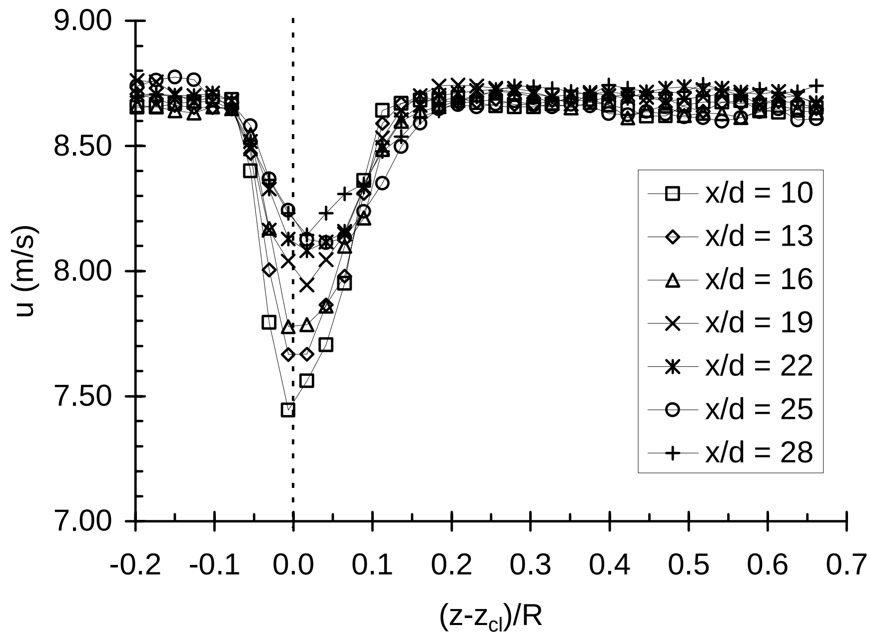

Figure 4.14: Mean velocity profiles from 5/16/02.

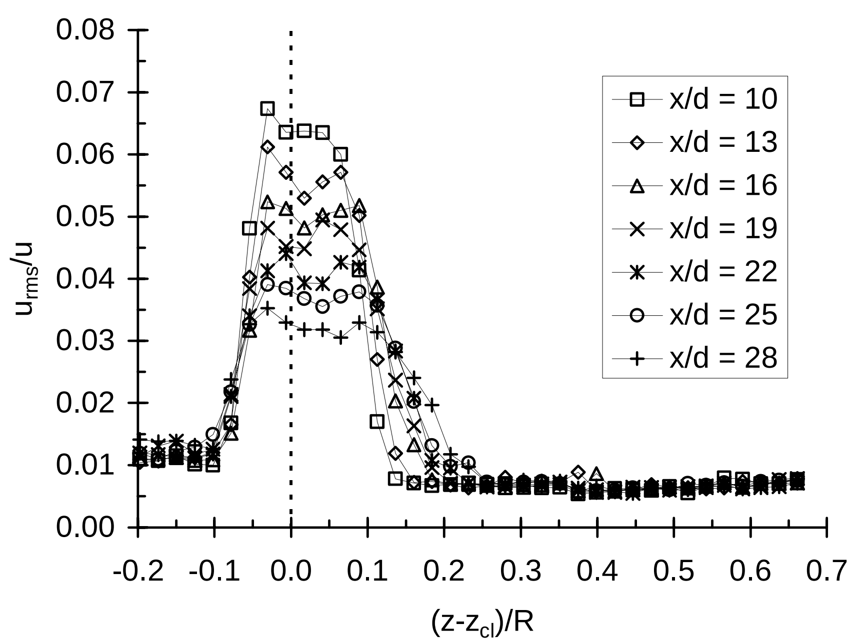

Figure 4.15: Turbulence intensity from 5/16/02.

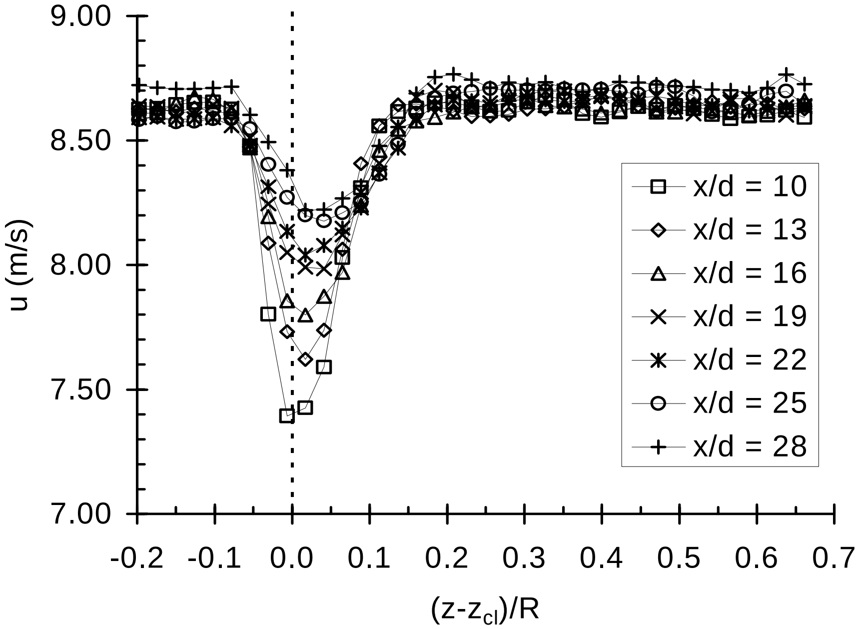

Figure 4.16: Mean velocity profiles from 5/17/02.

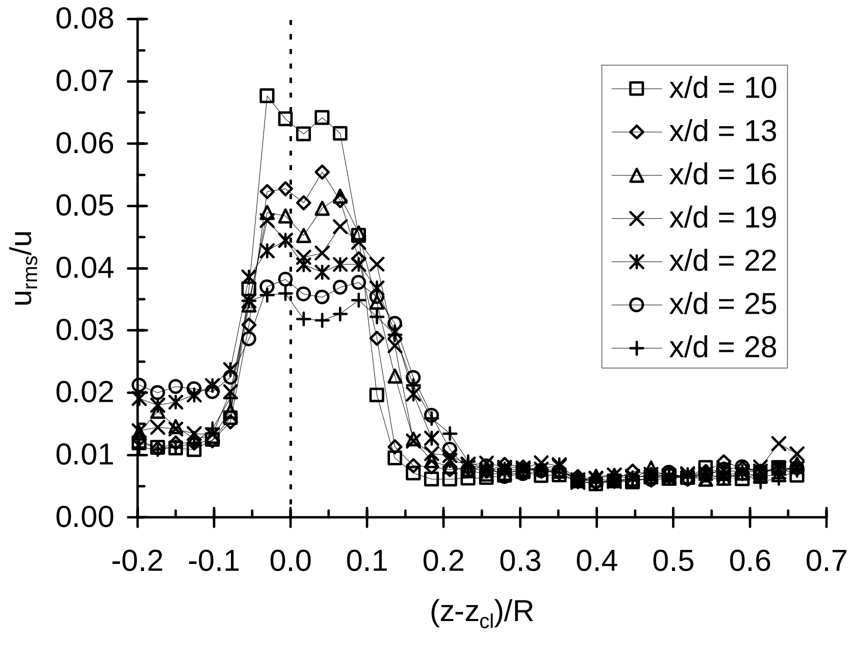

Figure 4.17: Turbulence intensity from 5/17/02.

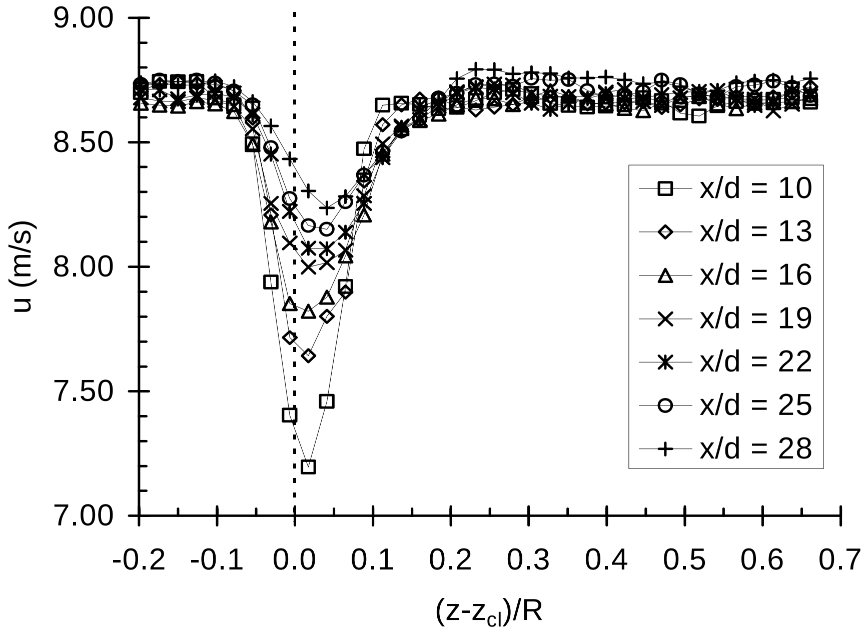

Figure 4.18: Mean velocity profiles from 5/22/02.

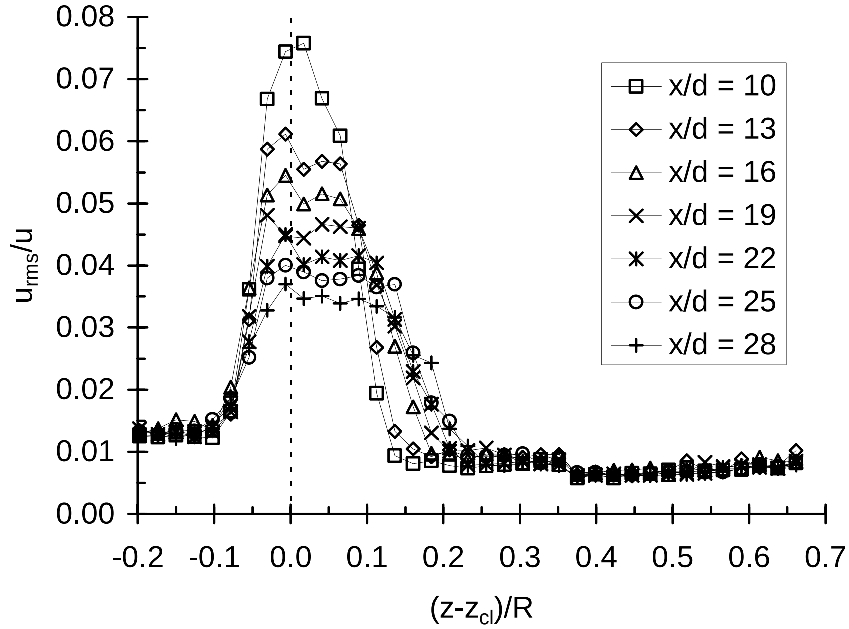

Figure 4.19: Turbulence intensity from 5/22/02.

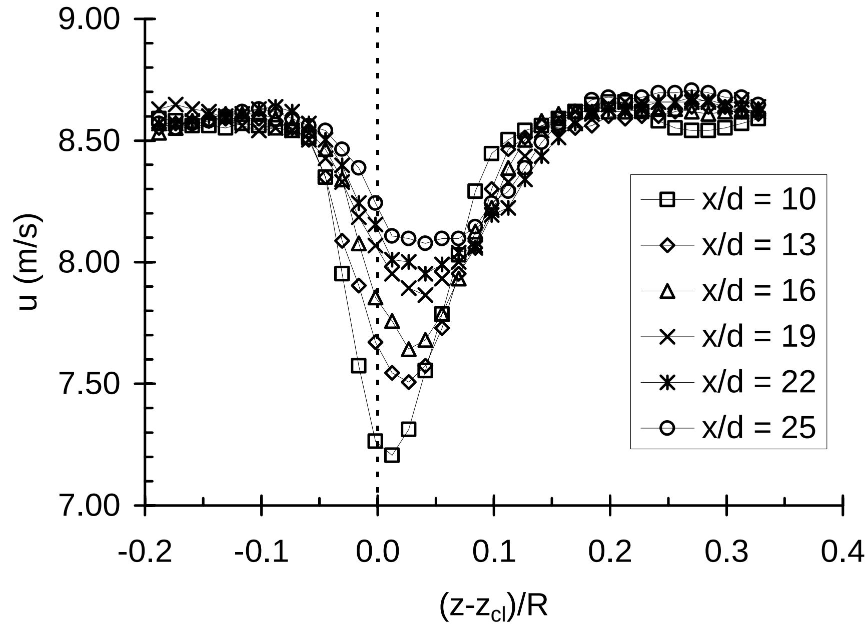

Figure 4.20: Mean velocity profiles from 5/30/02.

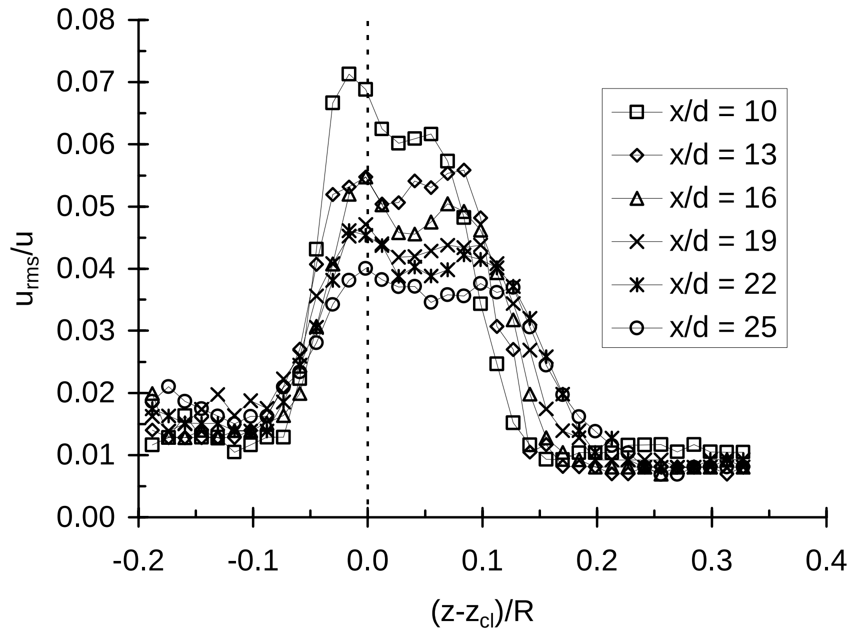

Figure 4.21: Turbulence intensity from 5/30/02.

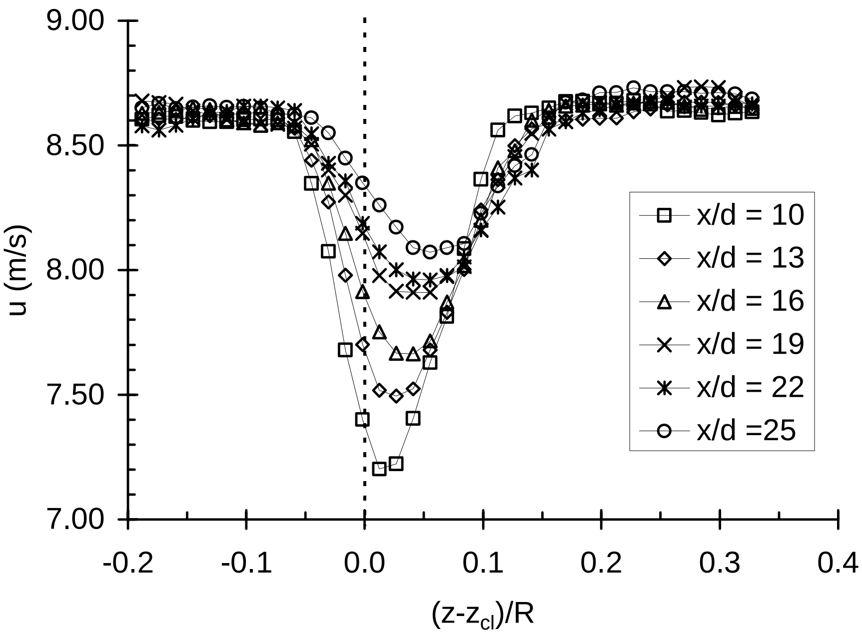

Figure 4.22: Mean velocity profiles from 6/4/02.

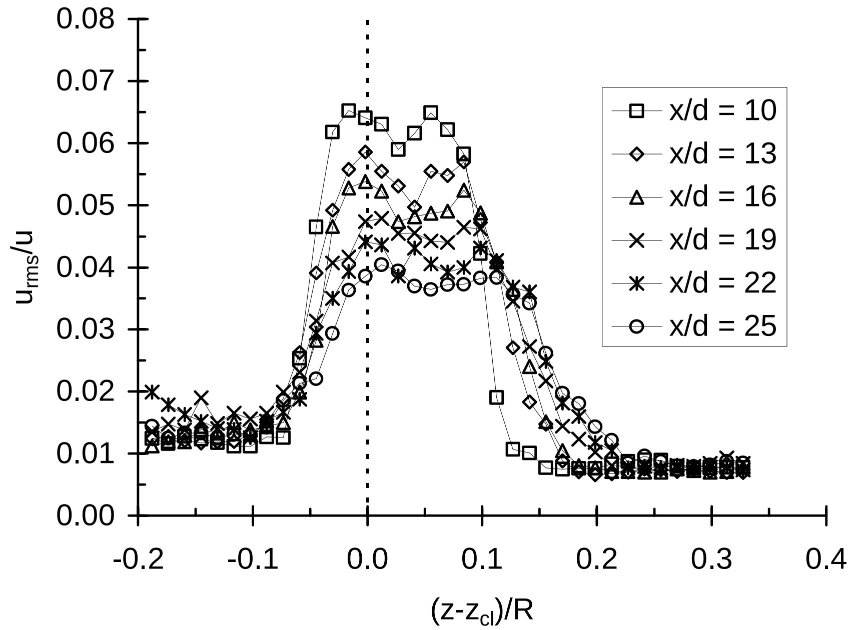

Figure 4.23: Turbulence intensity from 6/4/02.

The mean velocity profiles are asymmetric and are generally not centered along the measured centerline of the test section. The measurements of the wake beyond the centerline were characterized by higher turbulence intensity and lower data rates. The peculiar behavior of the velocity profiles suggests that the model was not aligned properly with the flow. After the model was mounted, the accuracy of alignment was checked and found to be within 0.5^{o}. However, previous studies had discovered that the test section becomes distorted when pressurized. According to measurements by Lindsey [6], the test section bulged 0.009 in (0.23 mm) when pressurized to 50 psi. It is possible that the deflection of the test section while under pressure caused a misalignment of the model with the mean flow. Also, it was observed during operation that the strut would occasionally deflect from side to side. These strut deflections may have contributed to the asymmetry of the wake profiles.

The wake centerline drift seen in the plots represents an offset of approximately 0.5^{o}. During later measurements of the test section wall surface irregularities, it was discovered that the traverse x-axis was misaligned by 0.7^{o} in the same direction as the centerline shift. This misalignment did not affect the final drag calculations as the wake centerline was corrected in the curve fitting process. The uncertainty that the angular misalignment imposed on the LDV velocity measurements was approximately ±0.007 m/s.

Figures 4.24, 4.25, and 4.26 illustrate the typical uncertainty associated with the velocity measurements. The data is taken from the series of measurements from 5/22/02, and at *x/d* = 10, 16, 25. The velocity and position error sources are taken to be the same as those used in the test section characteristic profiles.

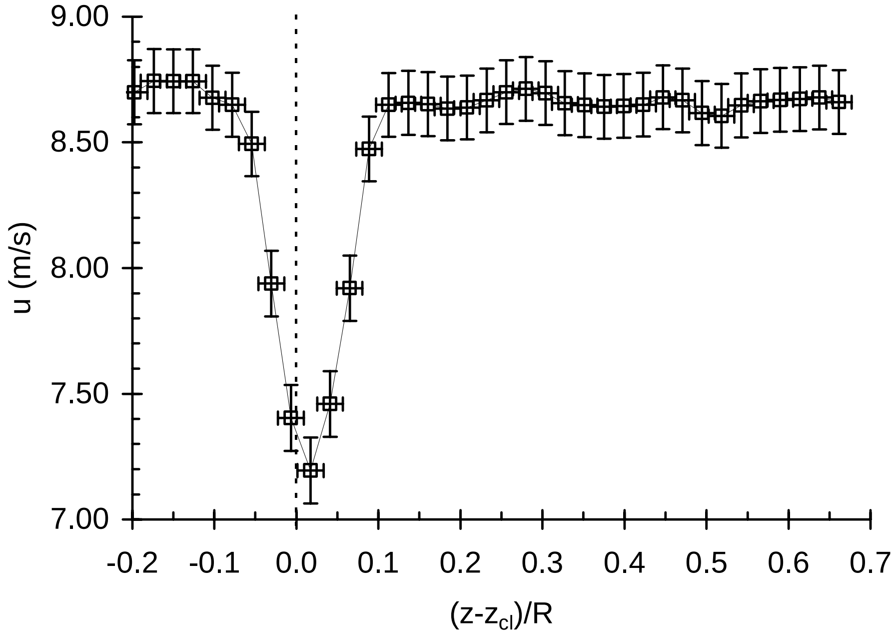

Figure 4.24: Velocity profile with typical uncertainties, 5/22/02, *x/d* = 10.

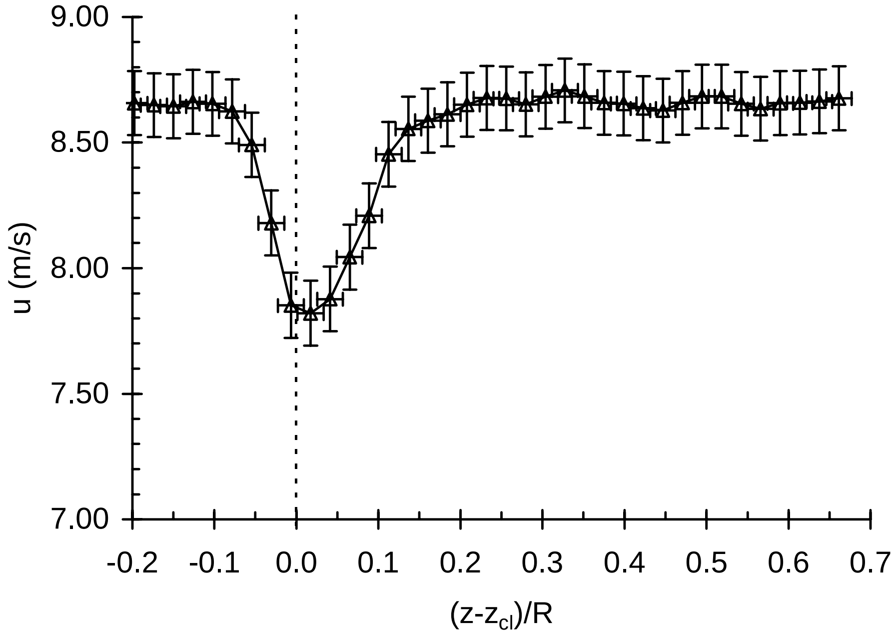

Figure 4.25: Velocity profile with typical uncertainties, 5/22/02, *x/d* = 16.

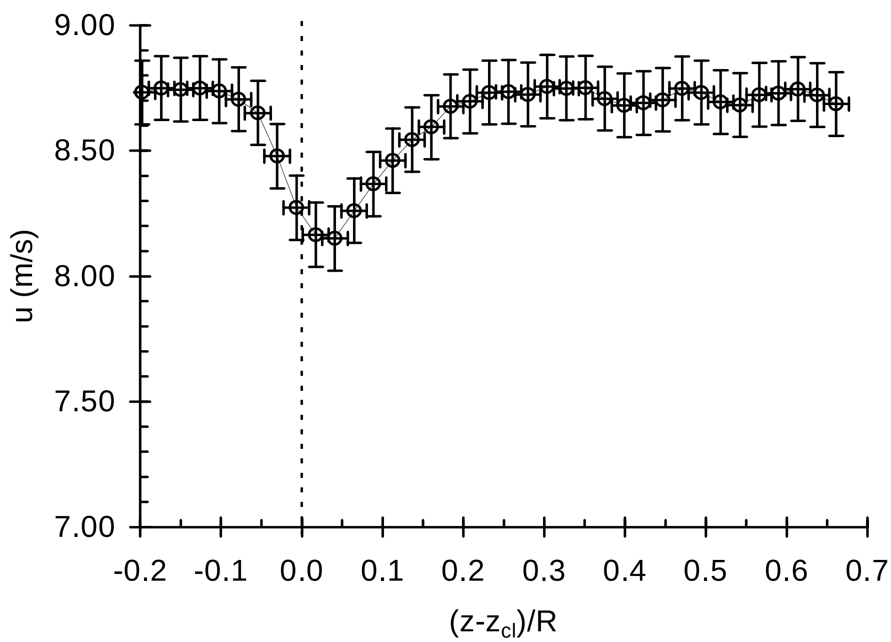

Figure 4.26: Velocity profile with typical uncertainties, 5/22/02, *x/d* = 25.

4.3.2 Curve Fits to Wake Profile Data

The wake profile data was fit using the numerical form of equation (2.59) so that the drag coefficient of the hull form could be calculated. The curve fits were done in MathCAD using the "genfit" function. The genfit function finds the least squares fit of an arbitrary function to a given data set. First, the wake velocity profile data *z* and *u* were read from a file and the Gaussian curve fit function was applied in the form:

$$u(z) = U_0 - u_0\, e^{\frac{-(z-z_0)^2}{b^2}} \tag{4.3}$$

where U_0, u_0, z_0, and *b* were generated from the curve fit. z_0 is the wake centerline location, *b* is the wake width parameter, u_0 is the velocity scale factor, and U_0 is the mean velocity outside of the wake. Since the curve fit process did not include the (ln 2) factor, the wake width parameter was corrected after the curve fit by dividing by $\sqrt{(\ln 2)}$. This curve fitting process was repeated for each x/d location.

After the wake curve fit was completed, the fits of length scale and velocity scale were performed to obtain the coefficients c_u and c_l that were introduced in equations (2.61) and (2.62). The set of data *x/d*, u_0, and *b* were again used with the genfit function to fit the velocity defect function:

$$\frac{u_0(x)}{d} = c_u\left(\frac{x-x_0}{d}\right)^{-2/3}. \tag{4.4}$$

The curve fit yielded c_u and x_0/d. The x_0/d value was then used in the function fit for the wake width parameter to find c_l :

$$\frac{b(x)}{d} = c_l \left(\frac{x - x_0}{d} \right)^{1/3}. \tag{4.5}$$

In order to use these power law fits, the measurements had to be made in a region of the wake where the velocity deficit and width parameters follow this behavior. In experiments conducted by Chevray [8], the wake of a 6:1 prolate spheroid achieved similarity at $x/d \approx 10$. All measurements in the current experiments were made at an $x/d \geq 10$, and since the submarine model had a larger fineness ratio than that of Chevray's spheroid, the wake of the submarine model should have been self-similar at all the measured positions. The self-similarity of the submarine wake profiles is illustrated in Figure 4.27 and Figure 4.28. The wake velocity profiles are clearly self-similar and fit the Gaussian function, although the region outside the wake is noisy in the 5/22/02 data.

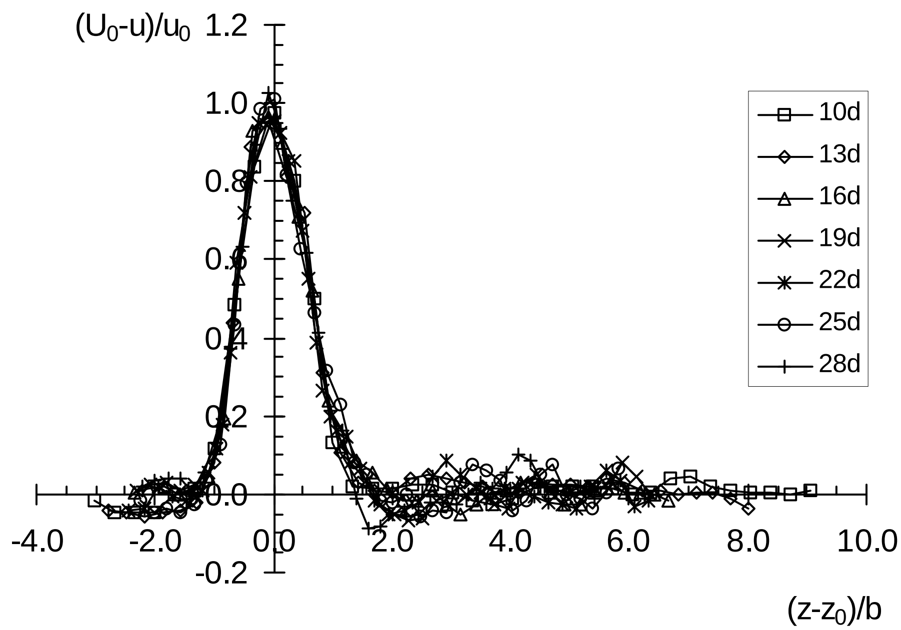

Figure 4.27: Similarity profiles for 5/22/02 data.

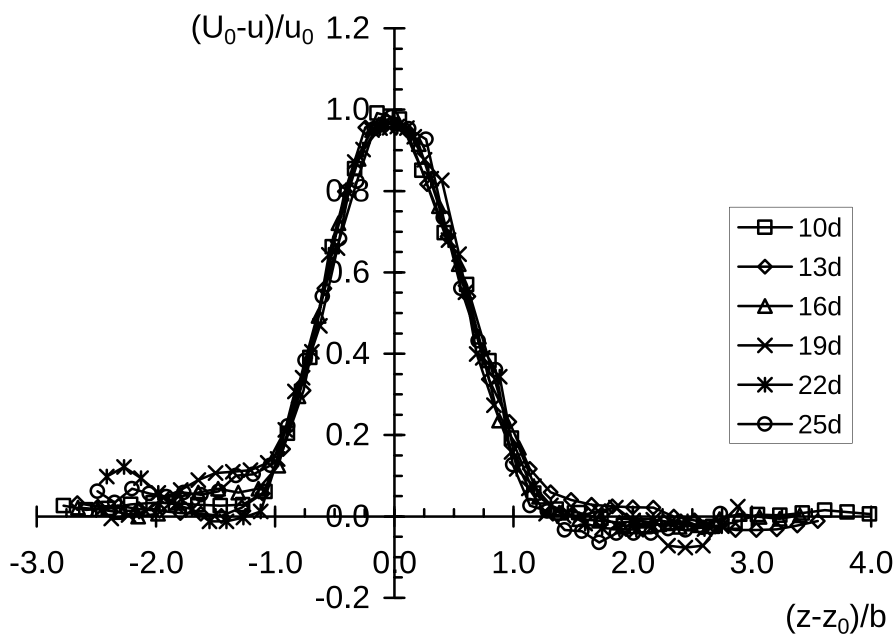

Figure 4.28: Similarity profiles for 6/4/02 data.

Figure 4.29 illustrates the variation of the freestream velocity U_0 outside the wake as x/d changes. The general trend is that U_0 increases as x/d increases; however, there are local variations in this trend that were not repeatable. Figure 4.30 plots the changes in nondimensionalized velocity deficit u_0/U_0 with x/d. The results are similar, if not consistent. Figure 4.31 plots the changes in the wake width parameter b/d over x/d. The fits are not very repeatable.

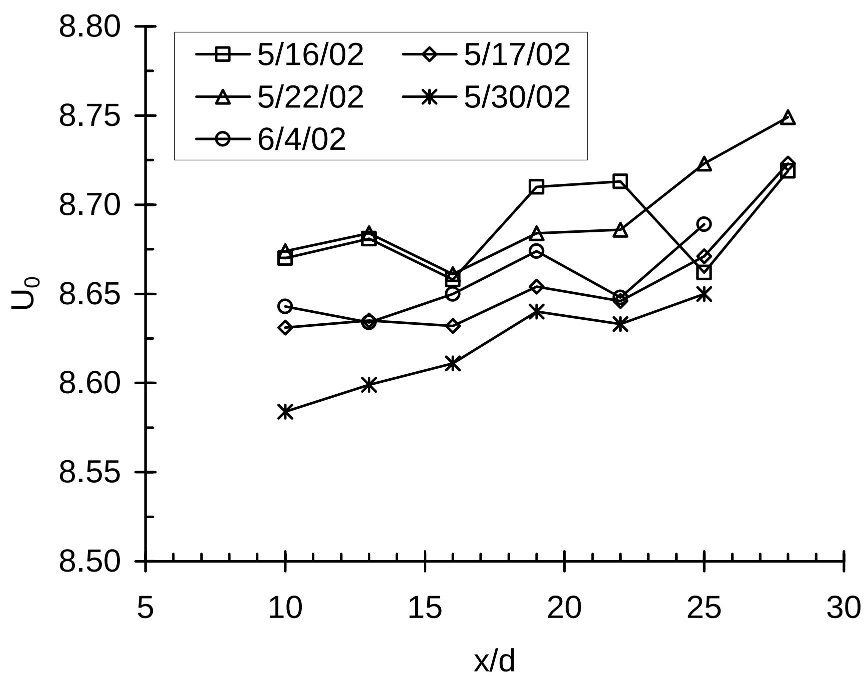

Figure 4.29: Freestream velocity U_0 outside of wake.

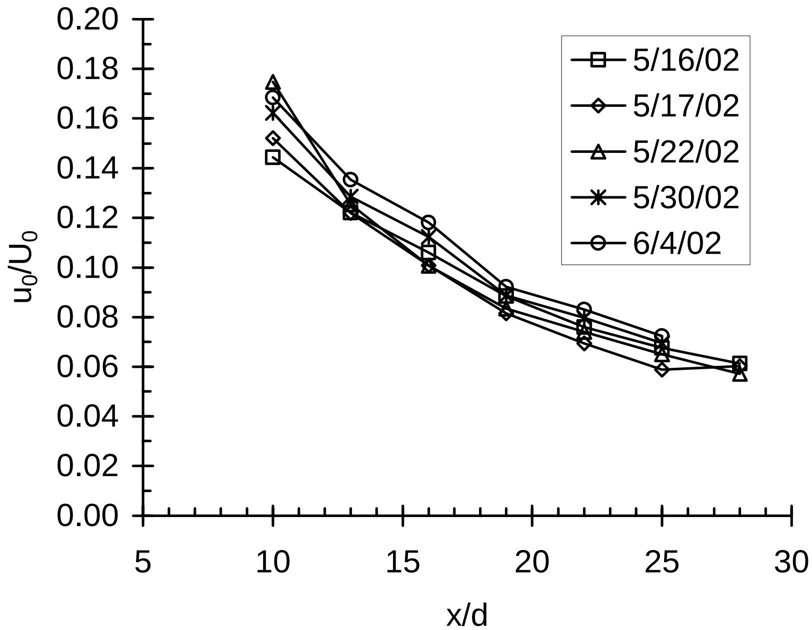

Figure 4.30: Velocity deficit u_0/U_0.

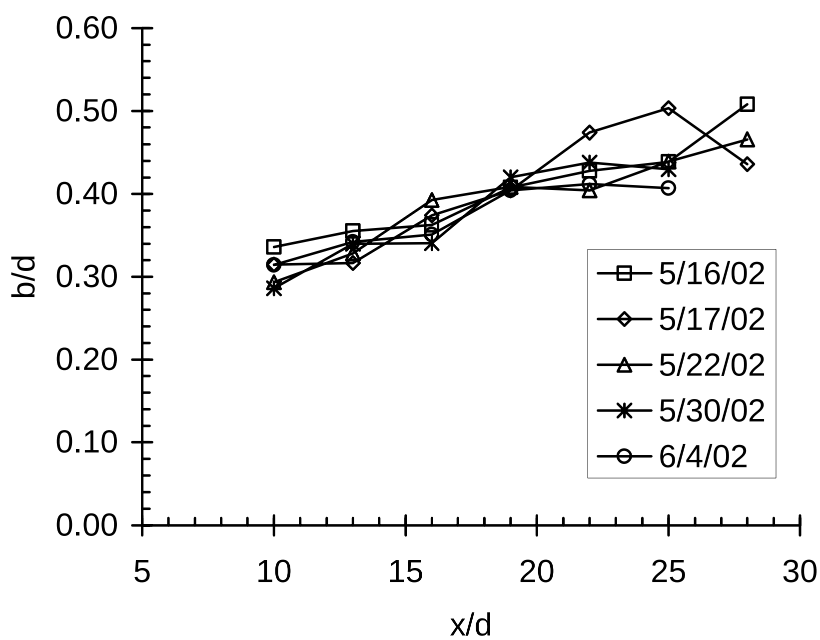

Figure 4.31: Wake width parameter *b/d*.

4.3.3 Drag Coefficient of Model

The drag coefficient may be calculated from each day's data through the use of equation (2.65). The drag coefficient can then be corrected for the pressure gradient that exists in the test section. This pressure gradient was measured by Lindsey [6] for various tunnel speeds. For a tunnel speed setting of 500 rpm, the pressure gradient is –0.0058 psi/in, with an uncertainty of ±0.0009 psi/in. The drag coefficient due to the pressure gradient is given by:

$$C_{D,p} = \frac{8F_p}{\rho \pi d^2 U_\infty{}^2}, \tag{4.6}$$

where F_p is the reaction force on the body due to the pressure gradient, and U_∞ is the freestream velocity as given by equation (4.1). The pressure reaction force F_p is found by multiplying the pressure gradient with the volume of the body:

$$F_p = \frac{dp}{dx} \mathcal{V}_{body}. \tag{4.7}$$

This is the standard form for the so-called "buoyancy drag" as reported in AGARDograph 109 [9]. The resulting pressure force in any case is approximately 0.04 lbf, and the resulting contribution to the drag coefficient is $\Delta C_{D,p} \approx 0.010$, where the reference velocity is U_∞ = 8.575 m/s.

The results of the fits are reported in Table 4.1. As can be seen, the results were varied and unrepeatable. The range of drag coefficients were from 0.122 to 0.351. The uncertainty in the drag coefficient due to the uncertainty in the pressure gradient is ±0.002. The drag coefficient was expected to be approximately 0.2. This expectation was based on previous experiments with the same model at the LCC and on computational studies by Cash [10]. The result that most nearly approaches the expected value is from the 5/16/02 data set; yet it is still 15.5% higher than the expected value.

Table 4.2: Curve fit results for each day's experiment.

Experiment Date	x_o/d	c_u	c_l	C_D (neglecting pressure gradient)	C_D
5/16/02	2.501	0.566	0.192	0.241	0.231
5/17/02	4.377	0.49	0.253	0.361	0.351
5/22/02	5.55	0.475	0.169	0.157	0.147
5/30/02	3.595	0.565	0.208	0.283	0.283
6/4/02	3.511	0.594	0.139	0.132	0.122

The test conditions varied from day to day, which may account for some of the scatter in the results. The data from 5/16/02 and 5/17/02 were some of the first measurements to be taken of the wake profiles. During these tests, the tunnel fill valve was not left open. The tunnel was pressurized to 50 psi, and then the fill valve was turned off. Normally, the tunnel would remain at constant pressure. However, it had been noticed that the water tunnel leakage had increased during the first tests. After the tests were completed on 5/22/02, it was noticed that the static pressure in the tunnel had dropped to 25 psi. This had not been observed before. It was decided to keep the fill line on for all the tests thereafter to keep the tunnel pressurized at 50 psi. The velocity profiles measured on 5/30/02 and 6/4/02 were taken under a constant pressure of 50 psi, and demonstrated distinct differences from the profiles of the three previous days, although the input speed of the motor was the same for all tests. This difference in behavior is illustrated in Figure 4.32.

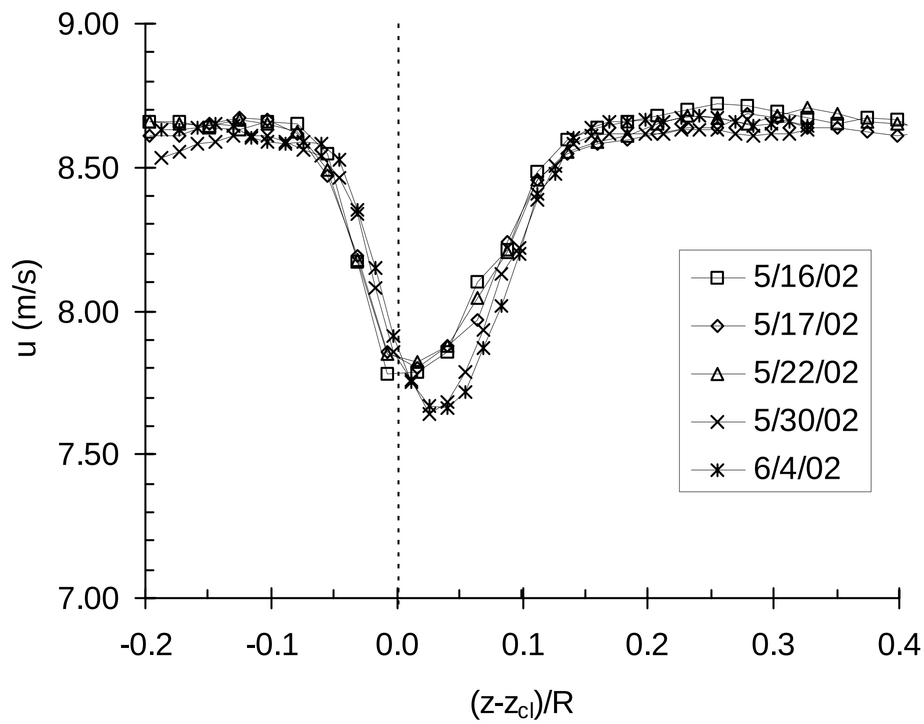

Figure 4.32: Comparison of wakes profiles at *x/d* = 16 for all five data sets.

After the wake measurements on 6/4/02, a study was performed to test the effect of decreasing pressure on the flow velocity within the test section. The LDV measurement volume was placed in the freestream and velocity measurements were taken continuously while the tunnel static pressure was allowed to bleed off from 50 psi to 25 psi. A plot of the time histories for the velocity and pressure readings is shown in Figure 4.33. The results were unexpected—the velocity fluctuated wildly with no apparent relation to the pressure drop. A similar test was performed with the tunnel fill valve left open, so that the tunnel remained at a constant static pressure of 46 psi. The results are shown in Figure 4.34. Except for a sudden drop in velocity observed near the beginning of the test, the velocity was fairly constant for nearly an hour. This test came to an abrupt end when the third corner of the water tunnel catastrophically failed under pressure. The failure prevented further study into the effects of decreased tunnel pressure and the velocity shifts that were noted earlier.

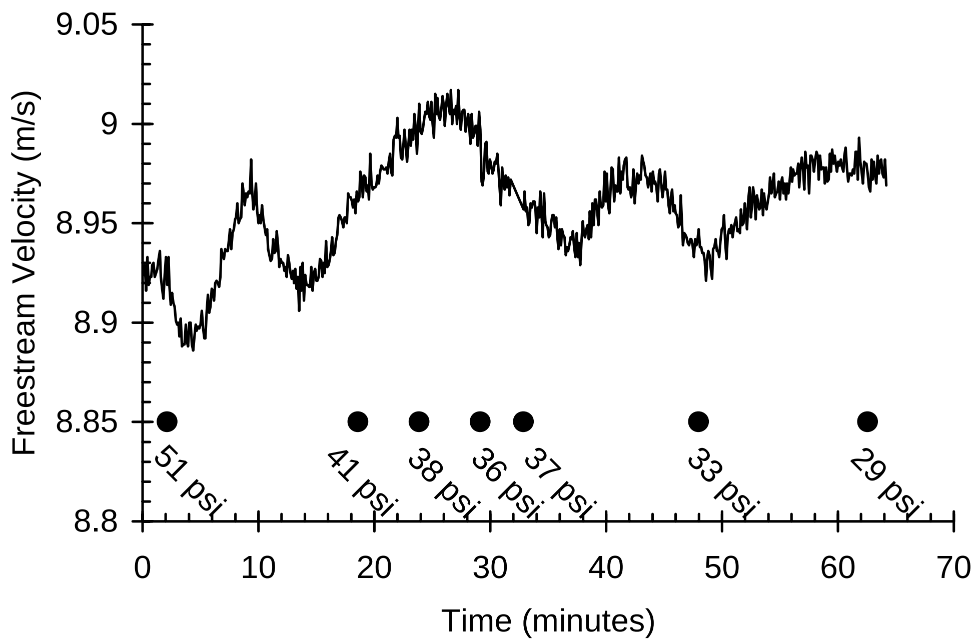

Figure 4.33: Test section freestream velocity behavior over a period of decreasing static pressure.

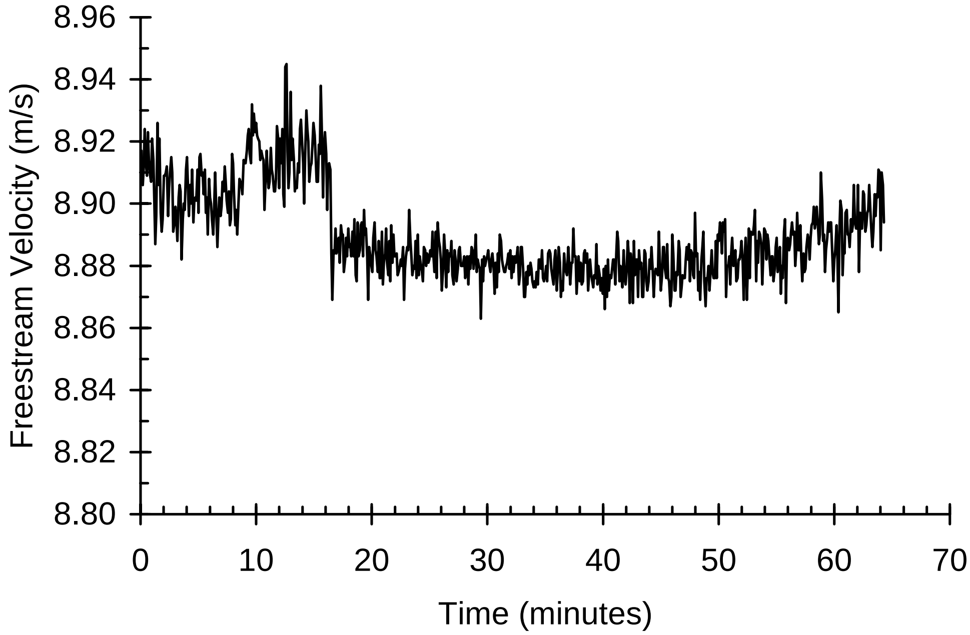

Figure 4.34: Test section freestream velocity behavior over a period of constant static pressure of 46 psi.

The profiles of 5/16/02 and 5/17/02 were taken under similar conditions. The tunnel water was seeded with 5-micron silicon carbide, which was found during the test section studies to improve data rates. However, with the presence of the model and its wake, the seeding was found to be detrimental. The water was drained after the tests on 5/17/02, and clean water was used on 5/22/02 and every day thereafter, with much better readings within the wake. The data taken on 5/16/02 and 5/17/02 were not originally intended to be analyzed and reported, but they were analyzed after the failure of the tunnel prevented any further testing to see if any other clues to the inconsistent measurements could be found. The tunnel pressure was not observed during the tests on

5/16/02 or 5/17/02. Another difference in operating conditions was the absence of shading from the overhead lighting, which was present from 5/22/02 and afterwards.

After 5/22/02, the fill line was left on during the tests to maintain the static pressure in the tunnel. The tests of 5/30/02 and 6/4/02 were run with constant static pressure of approximately 50 psi, consistent ambient lighting, and clean water. It was expected that these later tests would yield the most acceptable data. The drag coefficients from these later tests were 0.283 and 0.122, which are approximately 40% higher and lower than the expected drag coefficient of approximately 0.2.

To further explore the effect of the different operating conditions, the data was divided into two groups. The first three days' data represented the low pressure operating condition, and the last two days' data represented the high pressure operating condition. The velocity profile similarity parameters of the individual days' data were averaged to form composite velocity profiles representing the low pressure and the high pressure operating conditions. The power law fits were then applied to these two sets of data, as shown in Figure 4.35 through Figure 4.38.

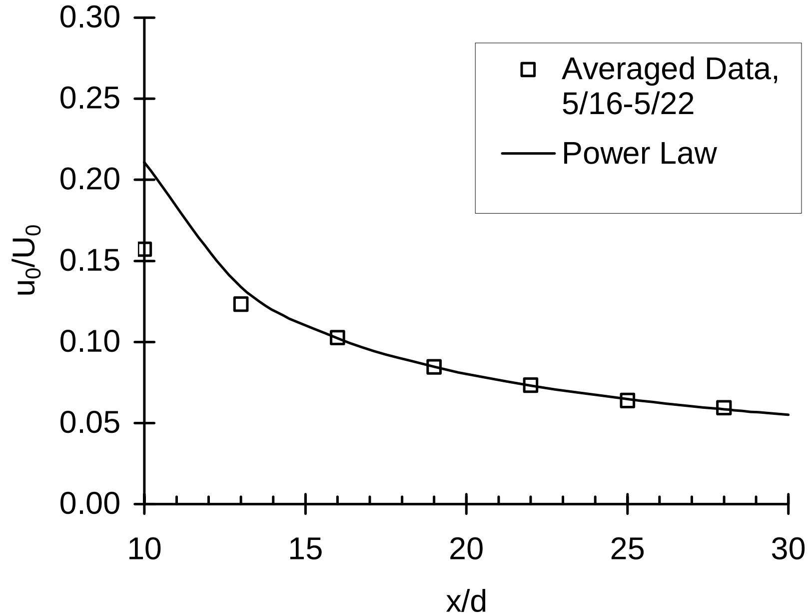

Figure 4.35: Comparison of averaged velocity deficit parameter from the first three days' experiments to the power law.

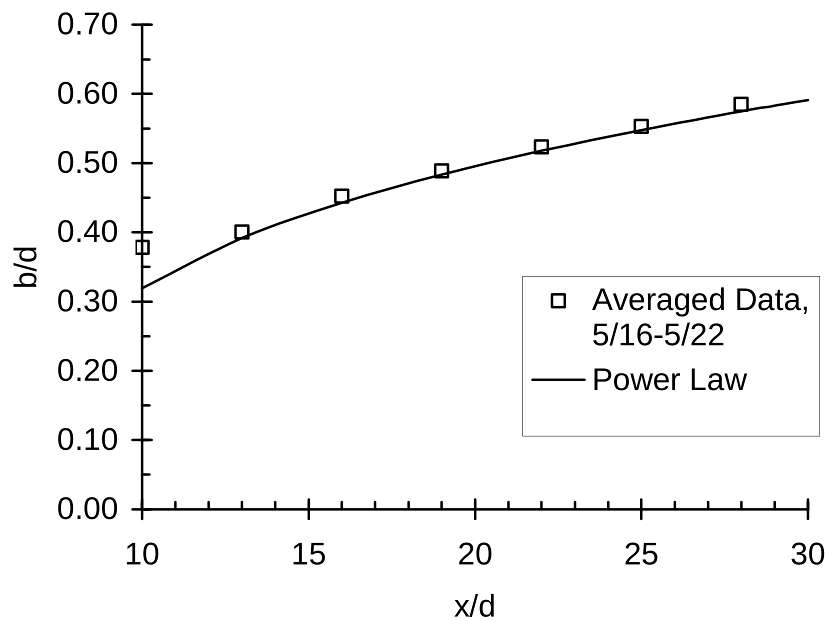

Figure 4.36: Comparison of averaged wake width parameter from the first three days' experiments to the power law.

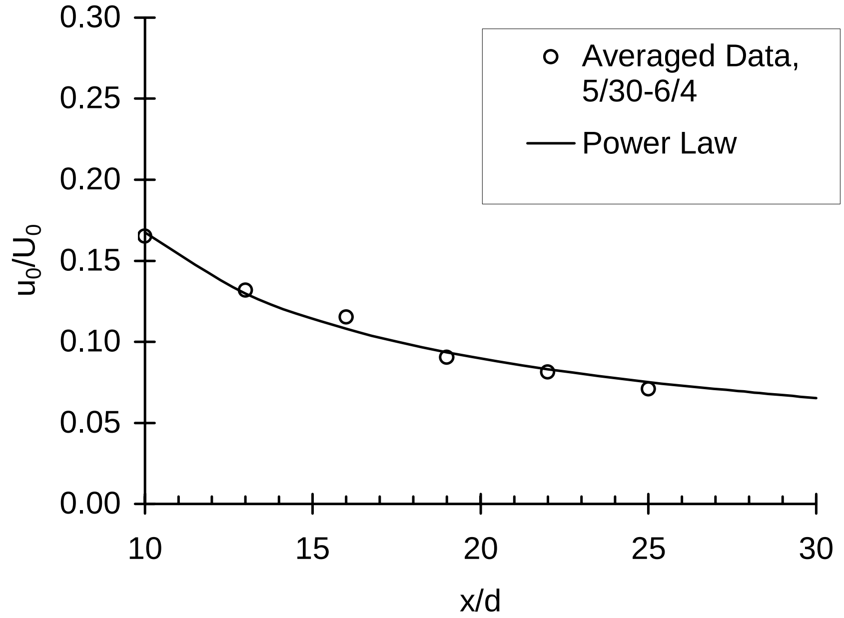

Figure 4.37: Comparison of averaged velocity deficit parameter from the last two days' experiments to the power law.

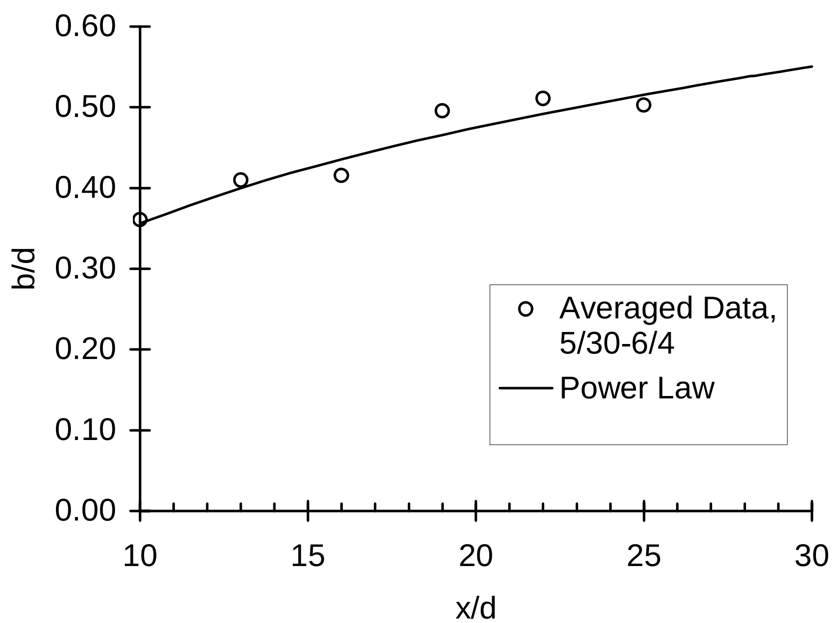

Figure 4.38: Comparison of averaged wake width parameter from the last two days' experiments to the power law.

The fits for u_0/U_0 and b/d for the composite decreased pressure measurements are very close to the forms that should be expected. For the composite constant pressure measurements, the fit for u_0/U_0 is fairly close to proper form, but the fit for b/d is erratic. The second fit parameters x_0/d, c_u, c_l and C_D are tabulated in Table 4.3. The drag coefficient results are very close to each other, and are in good agreement with the expected results from the LCC experiments and the computational results of Cash [10]. The computational results and the averaged experimental results for this hull shape are plotted in Figure 4.39. The individual and averaged experimental results are shown for two different temperatures, because the viscosity of water is very sensitive to the water temperature. The temperature of 20°C represents room temperature conditions. The temperature of 30°C is included because the water always seemed to be rather warm. No temperature of the water was taken, so the exact Reynolds number is unknown. Regardless, the averaged results are in good agreement with the trend of the computational results. This is again shown in Figure 4.40, which shows the averaged results along with Cash's computational results for three different submarine lengths.

Table 4.3: Curve fit results from composite data sets.

Experiment Date	x_o/d	c_u	c_l	C_D (neglecting pressure gradient)	C_D
Composite 5/16, 5/17, 5/22	6.930	0.445	0.195	0.195	0.185
Composite 5/30, 6/4	3.552	0.580	0.174	0.201	0.191

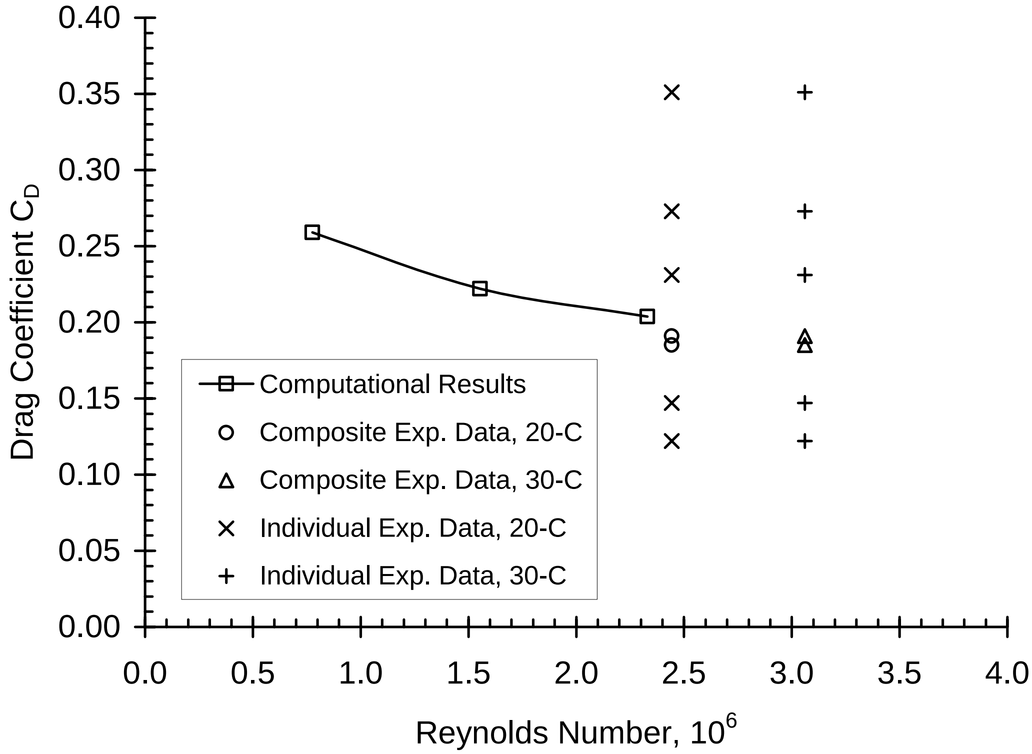

Figure 4.39: Comparison of experimental results with computational results of Cash.

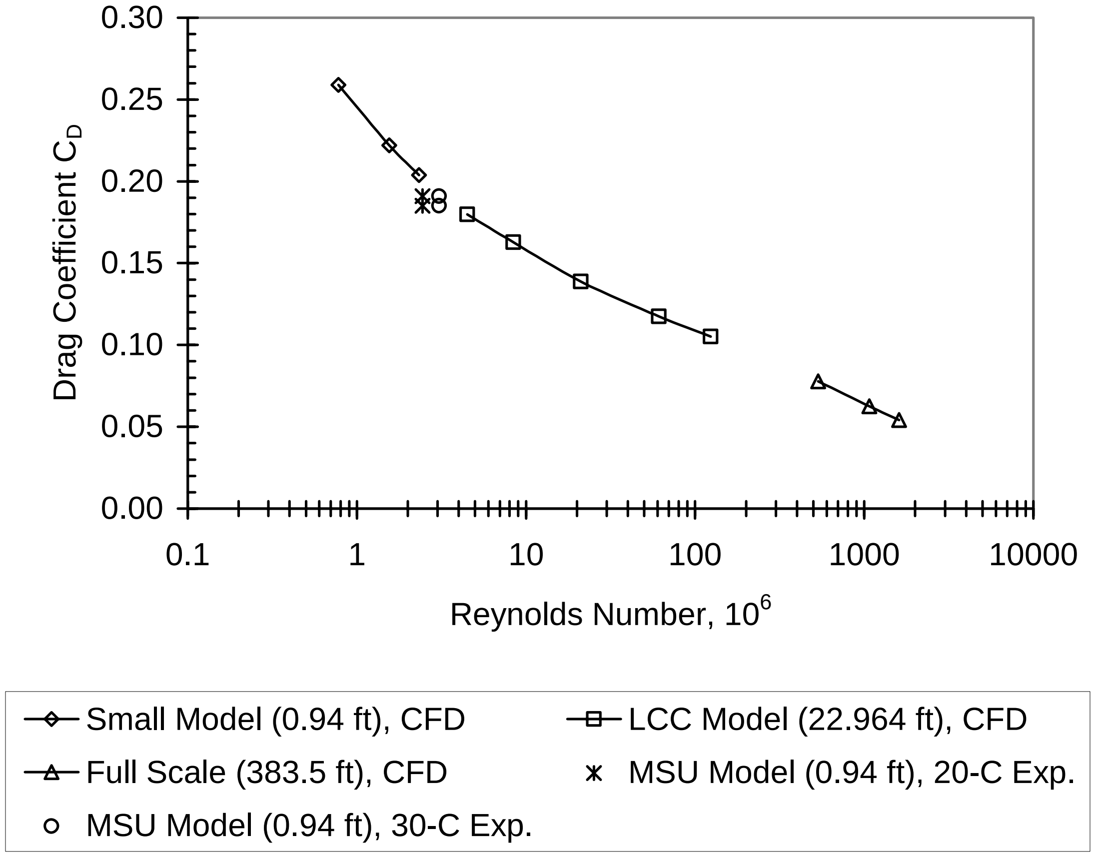

Figure 4.40: Averaged experimental results for MSU model and computational results of Cash for three different submarine lengths.

CHAPTER V

CONCLUSIONS AND RECOMMENDATIONS

5.1 Conclusions

The water tunnel was repaired after numerous problems developed after its last operational period. The corners of the water tunnel and the drive section were repainted with several coats of protective paint. The drive system of the tunnel was modified to solve a longstanding problem of bearing burn-out. After these renovations were completed, the water tunnel was run nearly daily for a period of two months.

A calibration device was constructed for the Aerospace Engineering Department's new LDV system. An uncertainty analysis of the calibration process was completed. Once calibrated, the LDV system was found to be accurate to within 0.75% for the velocity range of 5-10 m/s.

The water tunnel test section velocity profiles were measured with high accuracy using the LDV system. These velocity profiles are the first detailed measurements of the tunnel flow quality. Generally, the turbulence intensity of the freestream is 1.5%. A highly accurate tunnel speed curve was developed so that for a given motor input speed, the freestream velocity at $x/L = 0.125$ is accurately known. Also, it was discovered that the velocity profiles of the undisturbed freestream had repeatable kinks at a given x/L. These kinks are believed to have been caused by local optical properties in the Plexiglas® test section. During repeated measurements, it was noticed that the freestream velocity shifted occasionally by almost 0.5 m/s. The cause or possible period of this shift was not determined. It is possible that static pressure drop due to leakage was a cause, or that the LDV system had a faulty Bragg cell. The effects of tunnel pressure on velocity measurements were studied later after the measurements of the submarine wake had been completed. It was during these studies that the water tunnel ruptured under pressure.

An 11.278-inch long submarine model was mounted along the tunnel centerline. The wake velocity profiles were measured at 10, 13, 16, 19, 22, 25, and 28 body diameters downstream of the stern of the model on five different days. The velocity profiles exhibited asymmetry and a centerline shift. The velocity profiles were fit to a Gaussian function, and self-similarity parameters were obtained. The wake velocity profiles were found to be self-similar beyond $x/d = 10$. Power law fits were applied, and the drag coefficient of the submarine model was calculated. The individual data sets were very inconsistent, with C_D ranging from 0.122 to 0.351. However, when the data sets were combined into two sets, one representing measurements under decreasing tunnel pressure and one representing measurements under a high constant tunnel pressure, the drag coefficients were 0.185 and 0.191, respectively. Although no firm conclusions can be made about the drag coefficient results, it is believed that the distortion of the tunnel test section under high pressure may have caused the submarine model to become misaligned with the flow. This could have caused premature boundary layer separation and a higher drag coefficient as compared to the low-pressure results.

5.2 Recommendations

The third corner of the water tunnel must be repaired or replaced before the tunnel is operated again. There is a 2-ft long rupture in the fiberglass, as well as several bubbles in the inner coating. It is likely that water penetrated into the fiberglass, causing the layers to debond and thus weaken the structural integrity of the section. Since the bubbles are located throughout the damaged section, it is likely that water penetrated everywhere and the existing corner must be scrapped. Discussion with Raspet Flight Research Laboratory personnel who performed the repainting work revealed that the base coats did not adhere well to the tunnel parts. In light of this, all the corners and the drive section should be inspected for water damage.

Besides repair work, the one improvement that would greatly expand the research capability of the water tunnel would be to construct a rectangular test section so that the LDV is not restricted to velocity measurements on the horizontal plane of the centerline. This effect can be achieved by building a transparent box around the existing cylindrical test section, and filling it with water. A ray-tracing program may be needed if this is done, to account for four changes of media instead of only two.

A number of smaller modifications can be made to the water tunnel to expand its capability. A thermometer to measure the temperature of the water inside the tunnel would be useful for accurately determining Reynolds number for experiments. It is also recommended that the tunnel drive system be improved for smoother operation. It was found that the water tunnel vibrated excessively at operating speeds higher than 550 rpm. This limits the test section velocity to about 9.7 m/s (31.8 ft/s).

A more rigid and adjustable platform for the LDV traverse would also expand the measurement capability of the system. The current traverse can only cover half the length of the test section at one time. If the traverse were mounted on a platform that could be easily rolled while maintaining alignment with the tunnel test section, measurements could be made anywhere in the test section during a single period of testing. A rail-mounted platform is envisioned for this purpose, with the angular alignment of the rails being adjustable to remain parallel with the tunnel test section wall.

Finally, the LDV system needs to be examined to determine that it is in good working order. The sudden velocity shifts observed during the experiment may be due to the intermittent operation of the LDV Bragg cell. Successive measurements of a constant LDV calibration disk speed over a long period of time may show whether the velocity shifts in the data were caused by an anomaly in the LDV system or in the water tunnel.

BIBLIOGRAPHY

[1] Goldstein, S., ed., *Modern Developments in Fluid Dynamics: An Account of Theory and Experiment Relating to Boundary Layers, Turbulent Motion and Wakes*, Vol. 1, Dover Publications, New York, 1965.

[2] Dimotakis, Paul E., "Laser Doppler velocimetry momentum defect measurements of cable drag at low to moderate Reynolds numbers," Naval Construction Battalion Center, Contract No. N62583/77-M-R541, August 1977.

[3] Townsend, A.A., *The Structure of Turbulent Shear Flow*, Cambridge University Press, Cambridge, Great Britain, 1976.

[4] White, Frank M., *Viscous Fluid Flow*, McGraw-Hill Book Co., New York, 1974.

[5] Wells, Wm. Graham, "Design Principles for a High Speed Fiberglass Water Tunnel," Research Report No. 51, Aerophysics Department, Mississippi State University, April, 1964.

[6] Lindsey, Michael Lamar, "Renovation and Initial Operation of a High-Speed Water Tunnel," M.S. Thesis, Department of Aerospace Engineering, Mississippi State University, December 1998.

[7] Coleman, Hugh W. and W. Glenn Steele, Jr., *Experimentation and Uncertainty Analysis for Engineers*, John Wiley & Sons, Inc., New York, 1999.

[8] Chevray, R., "The Turbulent Wake of a Body of Revolution," *Journal of Basic Engineering*, June 1968, pp. 275-284.

[9] Garner, H. C., Rogers, E. W. E., Acum, W. E. A., and Maskell, B. C., "Subsonic Wind Tunnel Wall Corrections," AGARDograph 109, October 1966, pp.319-321.

[10] Cash, Allison Nicole, "Computational Studies of Fully Submerged Bodies, Propulsors, and Body/Propulsor Interactions," M.S. Thesis, Department of Aerospace Engineering, Mississippi State University, December 2001.